Separation of Na_V Subtypes in the Axon Initial Segment can Impede or Promote Backpropagation

Benjamin S.M. Barlow[a,1], André Longtin[a, b, c], and Béla Joós[a, b]

[a] *Department of Physics, University of Ottawa, STEM Complex, room 336, 150 Louis-Pasteur Pvt, Ottawa, ON, Canada, K1N 6N5*

[b] *Center for Neural Dynamics, University of Ottawa, Ottawa, Canada*

[c] *Department of Cellular and Molecular Medicine, Faculty of Medicine, University of Ottawa, 451 Smyth Road, Room 3206, Ottawa, Ontario, Canada, K1H 8M5*

[1] *To whom correspondence should be addressed. E-mail: BenjaminSBarlow@icloud.com*

April 1, 2022

1 Abstract

In a variety of neurons, action potentials (APs) initiate at the proximal axon, within a region called the axon initial segment (AIS) having favorable cable properties and a high density of voltage-gated ion channels. Pyramidal cells concentrate high-threshold sodium ion channels ($Na_V1.2$) in the proximal AIS, and the distal AIS contains mostly lower threshold $Na_V1.6$. It is widely believed that this separated Na_V distribution favors backpropagation and lowers the AP threshold. We implemented a range of hypothetical Na_V distributions in the AIS of a multicompartmental pyramidal cell model. Our simulations predict new effects on pyramidal neurons' excitability and backpropagation threshold, caused directly by the naturally occurring spatial separation of $Na_V1.2$ and $Na_V1.6$ in the AIS. By controlling the distribution of Na_Vs, pyramidal cells create a lengthwise profile of gating properties in the AIS. Using a "shift-clamping" technique, we demonstrate that different gating properties drive the effect of proximal $Na_V1.2$ on the backpropagation threshold when the neuron is stimulated somatically versus axonally. When stimulating current is injected at the soma, the intrinsic *right-shift* of $Na_V1.2$ *activation* causes these channels to raise the backpropagation threshold. However, with axonal stimulation, the *right-shift* of *availability* dominates, such that concentrating $Na_V1.2$ in the proximal AIS facilitates backpropagation. The latter effect is dynamic: *right-shift*ing steady-state *availability* is necessary but not sufficient to facilitate backpropagation; we show that the voltage-sensitive time constant of $Na_V1.2$ *availability* must be *right-shift*ed as well. Our results imply that regulation of Na_V separation can sensitively control backpropagation, especially for somatodendritic stimulation.

2 Significance Statement

Neurons use sodium ion currents, controlled by voltage-gated sodium channels (Na_Vs), to trigger electrical signals called action potentials (APs). APs propagate down the axon, and can backpropagate into the soma and dendrites where neurons receive synaptic input. Backpropagation is crucial for learning; neurons use this feedback to create and modify connections in the brain. The axon initial segment (AIS) triggers APs and backpropagation. In pyramidal neurons, the AIS contains two types of Na_V: high-threshold channels clustered near the soma where the AIS begins, and low-threshold channels near the end of the AIS. Our modeling predicts how this natural spatial separation of Na_V types can impede or promote backpropagation, and thus learning, depending on the site where the neuron is stimulated.

3 Main text

3.1 Introduction

In fluorescence microscopy images of neurons, the axon initial segment (AIS) is visible as a patch of axonal membrane near the soma with a high density of voltage-gated ion channels. These channels enable the AIS to initiate and shape action potentials (spikes) and regulate neuronal excitability Debanne et al. (2011). The AIS can be thought of as an organelle, that lives within the first $\approx 100\mu\mathrm{m}$ of axonal membrane and whose function is to supply the current needed to initiate spikes when the neuron decides to fire —usually in response to synaptic input. The AIS can move, up and down the axon and also change its length on a timescale of hours to days. This phenomenon called structural AIS plasticity enables neurons to optimize their sensitivity to specific input frequencies during development, and to homeostatically adjust their intrinsic excitability Adachi et al. (2015); Gulledge and Bravo (2016); Verbist et al. (2020). GABAergic input can also impinge on the AIS from axo-axonic synapses, such that the AIS can be modulated directly by interneurons. Fast AIS plasticity, including receptor-mediated changes to local ion channel properties and endocytosis of voltage-gated channels, occurs on timescales of seconds to minutes Petersen et al. (2017). (This is distinct from pathological remodeling induced by ischemia, although Vrselja et al. (2019) recently demonstrated that cortical neurons are more robust to interruptions in blood flow than previously thought.) The outsized electrophysiological influence of the AIS demands robust characterization of this short piece of axon as it interacts with its environment.

Over three-quarters of all neurons in the mammalian cortex are pyramidal cells, which have dendrites spanning the thickness of the cortex (several mm) and AIS lengths on the order of tens of $\mu\mathrm{m}$ Shepherd et al. (2019); Kole and Stuart (2012); Höfflin et al. (2017). In pyramidal cells, the AIS features an interesting distribution of voltage-gated sodium channels ($\mathrm{Na_V}$s): $\mathrm{Na_V}1.2$ channels cluster near the soma (i.e. at the proximal AIS) while $\mathrm{Na_V}1.6$ cluster toward the distal AIS Hu et al. (2009); Tian et al. (2014); Ye et al. (2018). The Hodgkin-Huxley kinetics of $\mathrm{Na_V}1.2$ are *right-shift*ed relative to those of $\mathrm{Na_V}1.6$ by an amount $V_{\mathrm{RS}} \sim 10 - 15\mathrm{mV}$ Rush et al. (2005). The AIS requires a high $\mathrm{Na_V}$ density to prime and initiate action potentials Mainen et al. (1995); Kole et al. (2008); Brette (2013). However, the purpose of the observed distribution of $\mathrm{Na_V}$ subtypes along the AIS remains unclear Katz et al. (2018); Spratt et al. (2021).

The observed $\mathrm{Na_V}$ distribution is reported to promote backpropagation —which is important for

learning— following axonal stimulation Hu et al. (2009), which could arise naturally from e.g. axo-axonic synapses. Backpropagated spikes drive learning by depolarizing the postsynaptic membrane, which triggers metabolic events that give rise to synaptic plasticity, including spike-timing-dependent plasticity. There is experimental evidence that postsynaptic backpropagation can release retrograde messengers into the synapse, and influence the future release of neurotransmitters from the presynaptic neuron Regehr et al. (2009). APs can influence calcium spikes in dendrites. And backpropagation can underlie bursting mechanisms in cortical neurons Mainen and Sejnowski (1996); Doiron et al. (2001), which makes it important for burst-dependent synaptic plasticity Payeur et al. (2021). Other computational powers are attributed to the AIS. Moving the initiation site away from the soma (i.e. toward the distal AIS) beyond a critical distance enables high-frequency spiking in cortical neurons, increasing the maximum spike frequency by an order of magnitude Brette (2013). Separating $\mathrm{Na_V}1.6$ into the distal AIS is said to push the initiation site toward that location, owing to those channels' lower voltage threshold Hu et al. (2009). However, Baranauskas et al. Baranauskas et al. (2013) showed that passive cable properties are sufficient to locate AP initiation at the distal AIS, in simulations having only one $\mathrm{Na_V}$ type.

Our modeling study is motivated by the following question: what effect does the separated spatial distribution of $\mathrm{Na_V}1.2$ and $\mathrm{Na_V}1.6$ in the AIS have on excitability and backpropagation? In particular, how does the finding of Hu et al. (2009) that the natural separation of $\mathrm{Na_V}$ subtypes favors backpropagation generalize to the more common situation of somatic stimulation? A natural approach is to systematically alter that $\mathrm{Na_V}$ distribution. We implement a variety of hypothetical $\mathrm{Na_V}$ density profiles in the AIS —presumably available to evolution— and compute the threshold for backpropagation in a biophysically detailed multicompartmental pyramidal cell.[1] Interestingly, we show here that $\mathrm{Na_V}$ separation enhances backpropagation with axonal stimulation but can impede it with somatic stimulation. This asymmetrical result was not expected.

To explain our results we independently modify the intrinsic V_{RS} of selected $\mathrm{Na_V}1.2$ gating variables and their respective time constants, by an amount ΔV_{RS} (i.e. $V_{\mathrm{RS}} \longrightarrow V_{\mathrm{RS}} + \Delta V_{\mathrm{RS}}$). These modifications to $\mathrm{Na_V}1.2$ properties are applied only in the AIS. Our selective ΔV_{RS} sweeps while clamping other variables to nominal V_{RS} values reveal that (I) $\mathrm{Na_V}1.2$ *availability* and its time constant explain how proximal $\mathrm{Na_V}1.2$ promotes backpropagation with axonal stimulation, and (II) the threshold of steady-state *activation*

[1] Cell geometry provided in Supporting Information, Figure S1.

explains how $Na_V1.2$ suppresses backpropagation and reduces excitability with somatic stimulation.

3.2 Results

3.2.1 Hypothetical Na_V distributions

The longitudinal distribution of AIS Na_V subtypes is smoothly transformed using the parameter x, from a natural distribution ($x = 1$) where $Na_V1.2$ and $Na_V1.6$ are spatially separated, into an artificial ($x = 0$) uniform mix of $Na_V1.2$ and $Na_V1.6$ (Figure 1a). Every distribution except the uniform Na_V mix has a location along the AIS at which the density of $Na_V1.6$ overtakes the $Na_V1.2$ density. That location, which we call the Na_V crossover and denote κ, is also varied in our simulations (κ is a dimensionless length normalized by the AIS length, Figure 1b). To cement our results, we will further apply identical transformations to the Na_V distribution in a fictional cell having a 'backward' AIS, that is with *proximal* $Na_V1.6$ and *distal* $Na_V1.2$. The backward AIS produces a mirror image of our findings.

For each hypothetical Na_V distribution, a short current pulse ($1\mathtt{ms}$) is injected at a specific site, and the minimum pulse amplitude required to elicit a spike is determined. Brief pulse durations separate the stimulation waveform from the intrinsic response of the cell, allowing threshold values to be given as the total injected charge, in picocoulombs ($\mathtt{pC}$). We define excitability in terms of two thresholds: backpropagation threshold Q_{BP} (AP leading to a spike in the distal dendrites), and forward-propagation threshold Q_{FP} (axonal AP with or without backpropagation). Current is injected either in the middle of the soma (somatic stimulation) or in the axon just distal to the AIS (axonal stimulation). Both are used by experimentalists Hu and Shu (2012), and certain pyramidal neurons are also known to receive axo-axonic input at the AIS as well as somatodendritic input Petersen et al. (2017). In both cases forward propagation refers to an AP traveling down the axon, and backpropagation always refers to an AP visibile as a spike in the dendrites (see Supporting Information, Figure S2).

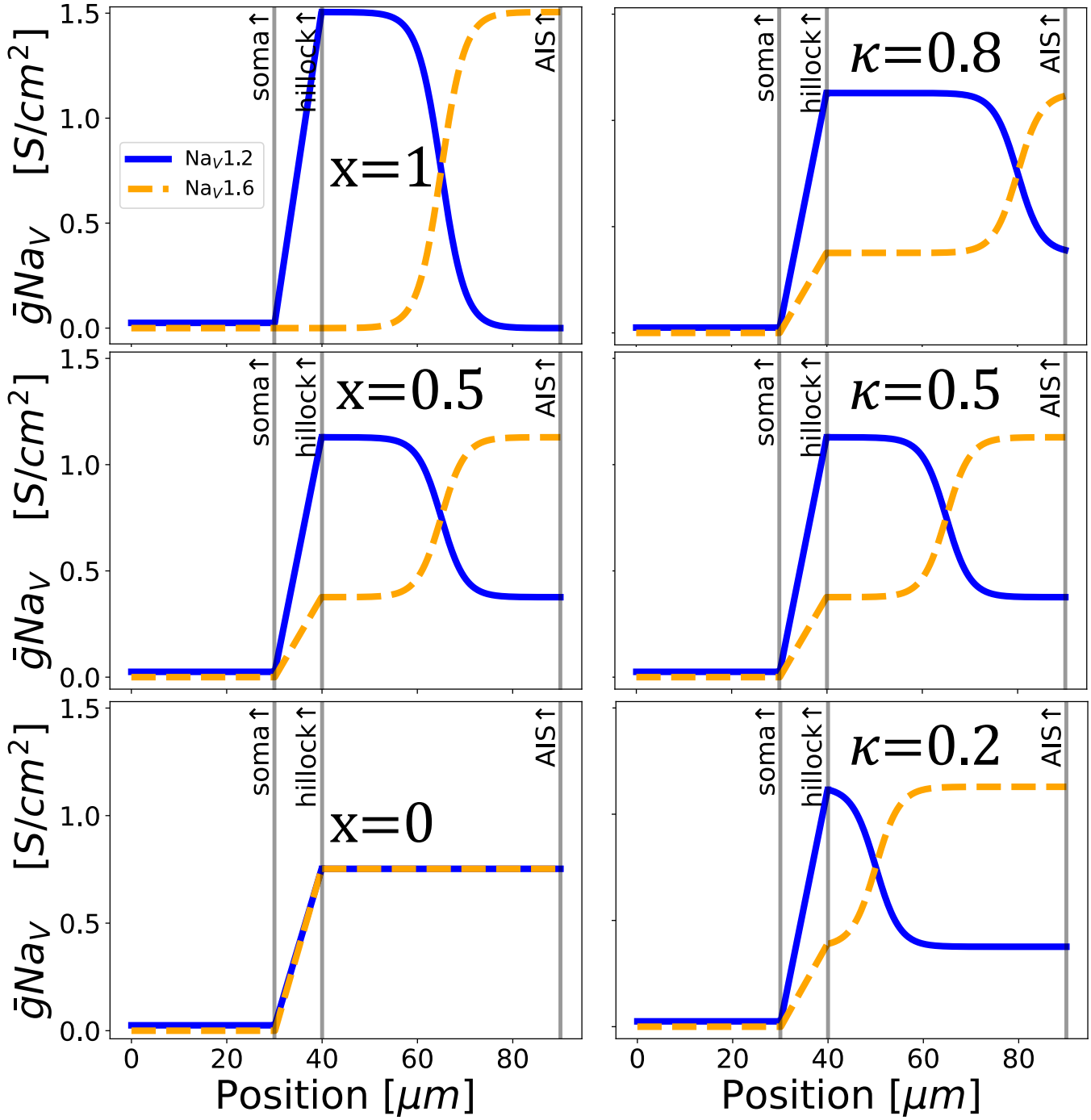

(a) (b)

Figure 1: Modifying the spatial distribution of Na_V subtypes in the AIS while keeping the total conductance constant. For visual clarity, we have lengthened the AIS to **50µm**. (a) The spatial separation of Na_V subtypes in the AIS is varied using the parameter "x" with $\kappa = 0.5$. The top plot is a model setup that mimics the observed distribution Hu et al. (2009) of Na_Vs in the AIS. The high threshold $Na_V1.2$ (indicated in blue) are concentrated close to the soma and the low threshold $Na_V1.6$ (indicated in orange) are kept distal to the soma. Moving from top to bottom, both Na_V subtypes are distributed ever more evenly along the AIS. We chose the parameter name "x" to vary the spatial separation of the AIS Na_V distributions because the natural distribution is x-shaped. Setting $x = 1$ in our simulations gives the natural distribution, and $x = 0$ gives the "flat" distribution wherein both Na_V subtypes are uniformly mixed. (b) Variation of the crossover location (κ) of Na_Vs in the AIS with $x = 0.5$.

3.2.2 Somatic stimulation

The standard AIS length in our model is 25 μm, based on measurements from Höfflin et al. (2017). In Figure 2 both negatively and positively sloped backpropagation threshold curves with respect to x are present, indicating that Na_V separation can promote or impede backpropagation (respectively). Changes in threshold can be as large as 30%. Moving the Na_V crossover (κ) toward the distal AIS shifts the backpropagation threshold curves upward. A qualitative change, namely the sign of the slope, occurs around $\kappa = 0.4$.

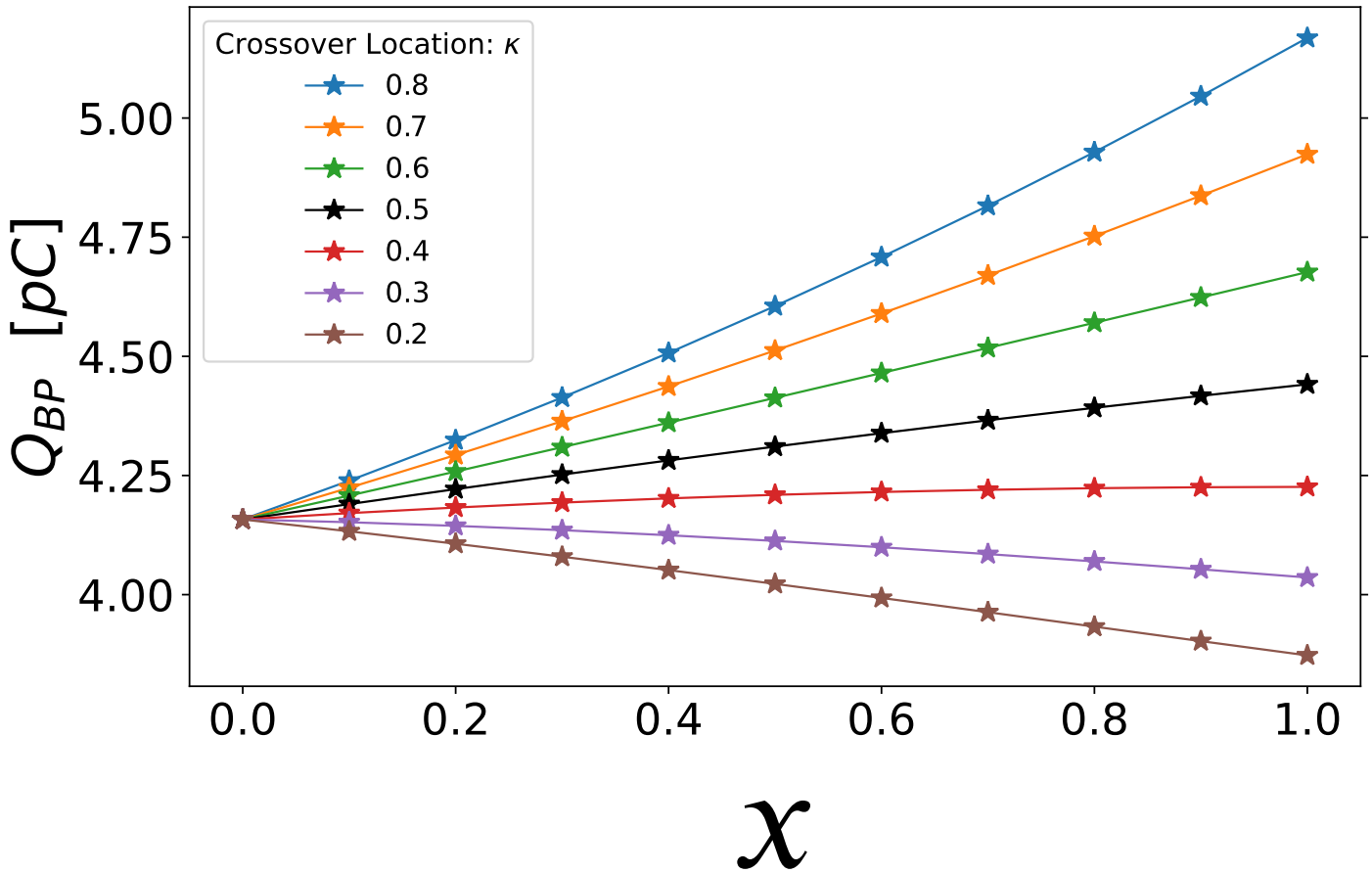

Figure 2: Somatic Stimulation: Combined effect of varying crossover location (κ) and Na_V separation (x) in the axon initial segment. The threshold for forward AP propagation is the same as for backpropagation. Varying the separation parameter "x" from $x = 0$ to $x = 1$, the distribution of Na_V channels goes from flat (artificial) to separated, the latter approximating the distribution observed in nature (see Figure 1a). Note that curves for all values of κ converge to a single point at $x = 0$, since κ can have no effect when the two Na_V's are uniformly distributed along the AIS. The lines have been drawn to guide the eye.

An intuitive explanation for this latter effect is that moving the crossover location away from the soma causes the AIS to be dominated by $Na_V1.2$ channels (see Figure 1b, $\kappa = 0.7$) which have a higher voltage

threshold than $Na_V1.6$. APs still initiate in the distal AIS but the dominant $Na_V1.2$ renders the cell less excitable. Further, for $\kappa \gtrsim 0.4$ the backpropagation threshold increases as we tend toward the natural x-shaped distribution of Na_Vs. This behavior is the opposite of what is observed for axonal stimulation, below and in Hu et al. (2009). We repeated these simulations with AIS length up to $100\mu m$ (Figure S4), and also with stimulation at the main apical dendrite (Figure S5) instead of the soma, and obtained the same qualitative results as Figure 2 (see Section S1.4).

The negatively sloped curves do not necessarily imply that proximal $Na_V1.2$ promotes backpropagation in the case of somatic stimulation. In those curves ($\kappa \lesssim 0.4$) the AIS is mostly populated with $Na_V1.6$ when $x > 0$. Also note that decreasing κ places more $Na_V1.6$ channels nearer to the soma (see Figure 1b, $\kappa = 0.2$). In that case, the threshold-lowering effect of Na_V separation could come from the increased $Na_V1.6$ density that results from increasing x when κ is relatively small, rather than from the proximal accumulation of $Na_V1.2$ with increasing x. (This is verified in Figure S4.) Further, increasing κ (which increases the ratio of $Na_V1.2$ to $Na_V1.6$ in the AIS) raises the threshold for all curves in Figure 2 regardless of slope (see Figure S3). Negative slopes vanish when the hillock is lengthened from $10\mu m$ to $30\mu m$ (Figure S6). It is then consistent to postulate that for somatic stimulation, the backpropagation threshold is increased by AIS $Na_V1.2$ at all values of x and κ, and Figure 2 is consistent with AIS $Na_V1.6$ enhancing excitability and backpropagation. In other words, for **somatic stimulation**:

- when $\kappa < 0.5$ and $x > 0$, the AIS is dominated by $Na_V1.6$: increasing x increases the proportion of total AIS Na_V conductance due to $Na_V1.6$ (negative slope: natural separation has lowest backpropagation threshold).

- when $\kappa > 0.5$ and $x > 0$, the AIS is dominated by $Na_V1.2$: increasing x decreases the proportion of total AIS Na_V conductance due to $Na_V1.6$ (positive slope: natural separation has highest backpropagation threshold).

The forward propagation threshold for somatic stimulation is not included in a separate figure since it is identical to the backpropagation threshold in this model. This does not depend on the somatic injection site.

An informative variation on Figure 2 is shown in Figure 3c in which the AIS is "put on backward", such that $Na_V1.6$ is proximal to the soma and $Na_V1.2$ is concentrated in the distal AIS. As one might

expect, the effect of varying χ and κ in Figure 3 is opposite to what is seen in Figure 2, albeit with some new curvature at low κ. This reinforces the observation that proximal $Na_V1.6$ facilitates backpropagation with somatic stimulation.

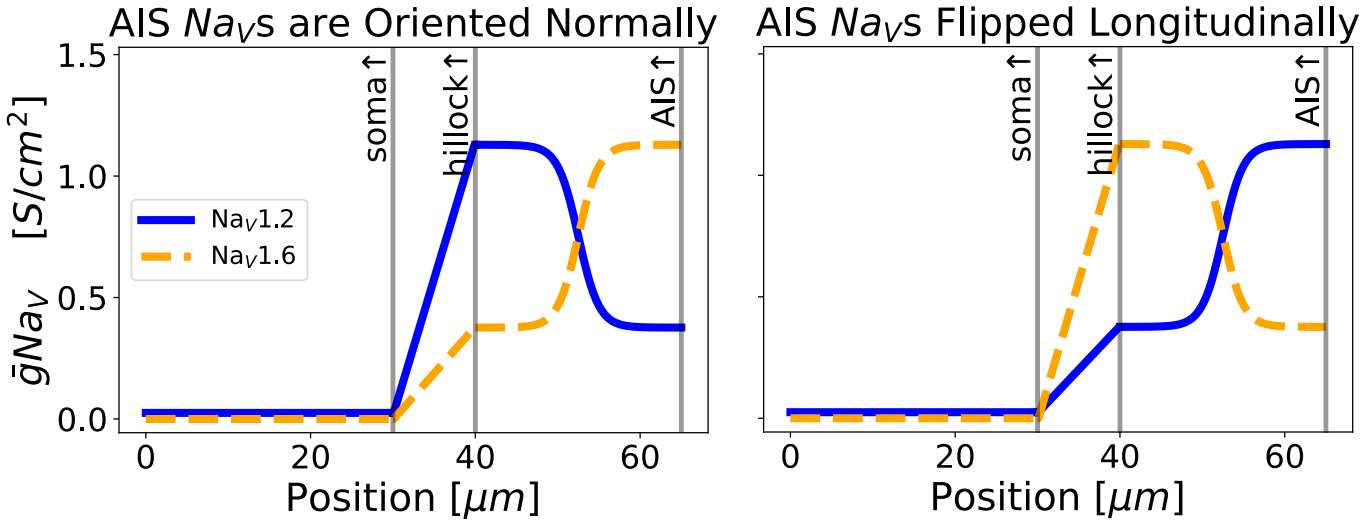

(a) (b)

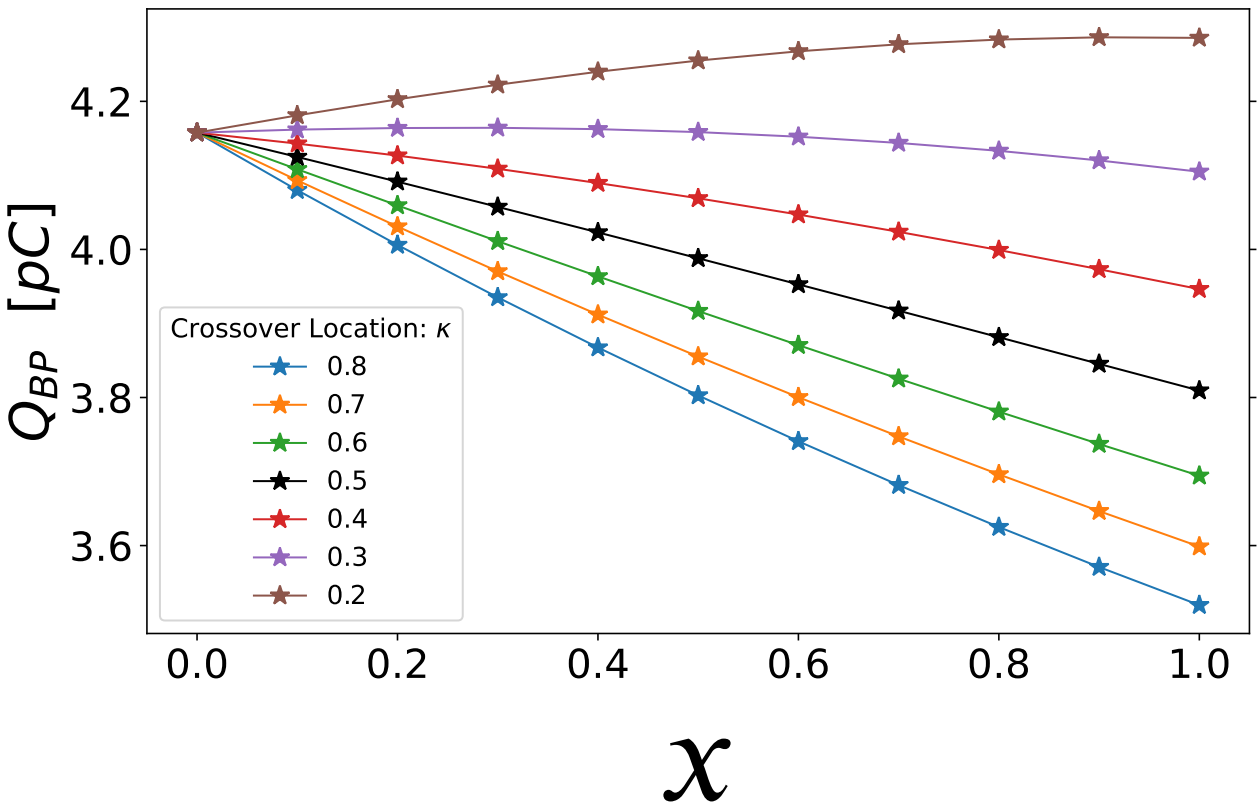

(c)

Figure 3: When the AIS Na_V distribution is flipped, setting $x = 1$ concentrates $Na_V1.6$ at the proximal AIS and $Na_V1.2$ at the distal AIS —the opposite of what is observed in many pyramidal cells Hu et al. (2009); Tian et al. (2014); Ye et al. (2018). (a) AIS with natural longitudinal placement of Na_Vs. (b) AIS with longitudinally flipped Na_V distribution. In both plots $x = 0.5$ and $\kappa = 0.5$. (c) Somatic stimulation with AIS Na_Vs flipped as in (b): This result is close to a mirror image of Figure 2. The lines have been drawn to guide the eye.

3.2.3 Axonal stimulation

With axonal stimulation (current injection just distal to the AIS), Na_V separation consistently lowers the backpropagation threshold (Figure 4). Contrary to somatic stimulation (Figure 2), moving the Na_V crossover (κ) toward the distal AIS shifts the backpropagation threshold curves downward.

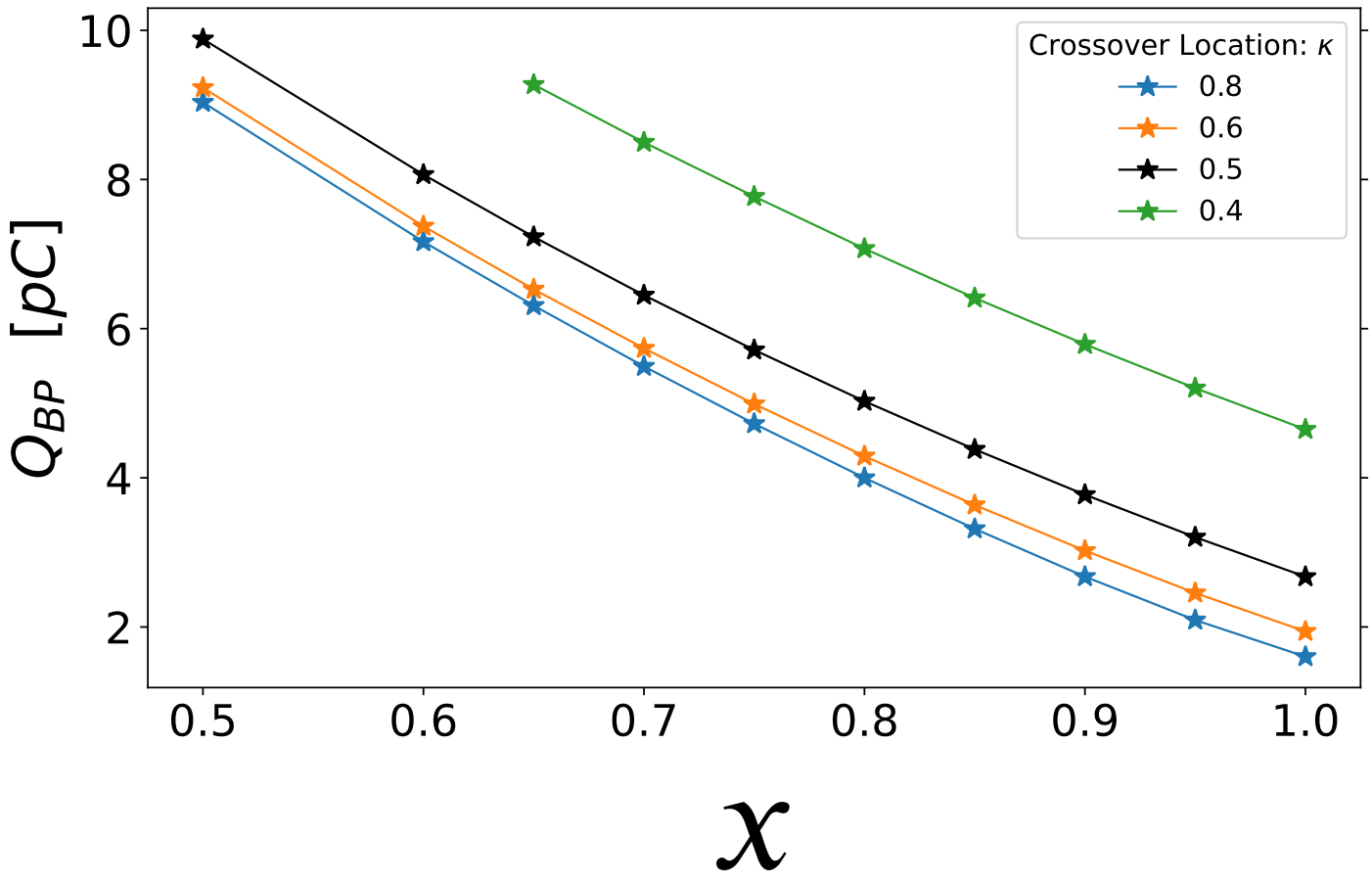

Figure 4: Axonal Stimulation: Effect of varying crossover location (κ) and Na_V separation (x) in the AIS on backpropagation threshold. Separating the two Na_V subtypes ($x \longrightarrow 1$) lowers the threshold, in agreement with Hu et al. (2009) who found that proximal accumulation of $Na_V1.2$ promotes backpropagation, albeit due to different gating properties (Figure 6a). Increasing κ raises the proportion of $Na_V1.2$ (relative to $Na_V1.6$) in the AIS and lowers the backpropagation threshold as well. Threshold changes here are larger than for somatic stimulation (Figure 2). When computing the threshold at different values of x and κ, the stimulating current was limited to a maximum of $10\mathtt{nA}$. To achieve backpropagation within that constraint (following axonal stimulation), our model required some amount of proximal $Na_V1.2$, delivered through the combined effects of Na_V separation ($x \gtrsim 0.5$) and a sufficiently distal crossover position $\kappa \gtrsim 0.4$. The lines have been drawn to guide the eye.

The decreasing threshold with respect to x in Figure 4 is consistent with Hu et al. (2009), who used axonal stimulation, in that proximal $Na_V1.2$ in the AIS promotes backpropagation. Our results for κ pro-

vide new support for their observations. This agreement is interesting because our approach to modifying the AIS Na_V distribution (described above in Figure 1) is quite different from their method which scales the density of $Na_V1.2$ by a constant, leaving the $Na_V1.6$ profile intact. We expect such scaling to have the same effect in our model since increasing or decreasing the density of $Na_V1.2$ in a separated distribution with a specified κ and $x > 0$ would scale the total AIS Na_V conductance, especially at the proximal AIS.

The forward-propagation theshold Q_{FP}, also referred to as the AP threshold, is shown in Figure 5. Stimulation amplitude is an order of magnitude lower than in the case of the backpropagation threshold. This is expected with axonal stimulation due to the high Na_V density of the distal AIS, its electrical isolation from the soma, and its proximity to the stimulus. Na_V separation concentrates $Na_V1.6$ in the distal AIS making it more excitable in the portion nearer to the stimulation site. This finding is consistent with Hu et al. (2009) who found that distal $Na_V1.6$ density places the lowest initiation threshold (and therefore the AP trigger zone) at the distal AIS. However, Baranauskas et al. (2013) has shown that cable properties are sufficient to explain why the trigger zone is located at the distal AIS (see Discussion). Moving the crossover distally ($\kappa \longrightarrow 1$) increases the total proportion of $Na_V1.2$ in the AIS, and thereby raises Q_{FP} threshold due to activation right-shift (see Figure 6).

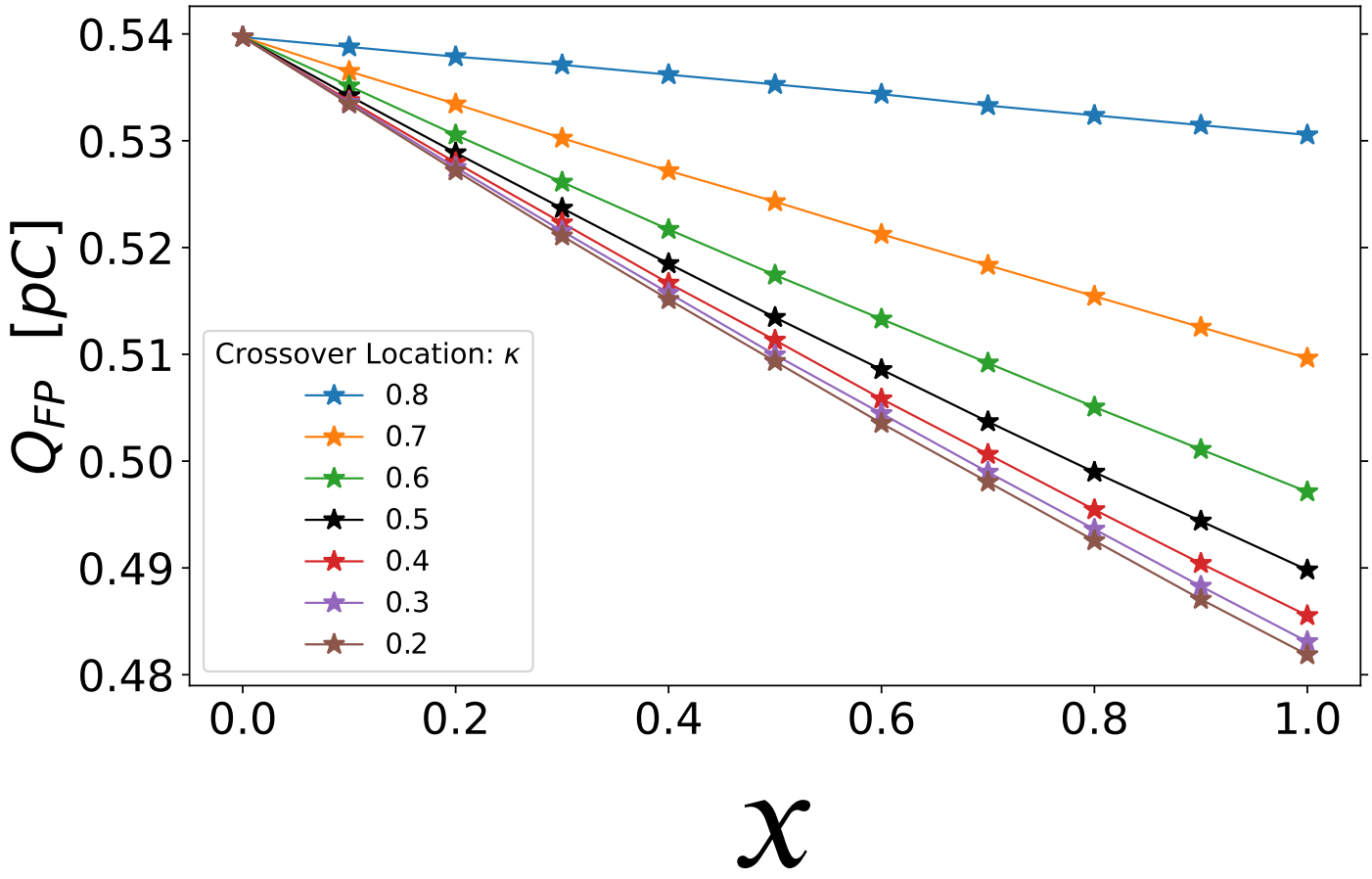

Figure 5: Axonal Stimulation: Effect of x and κ on forward propagation threshold. The trend for all constant κ curves is that a higher proportion of total AIS $Na_V1.6$ or a higher density of distal AIS $Na_V1.6$ lowers the threshold to initiate forward propagating action potentials. Note that this threshold is not sufficient to achieve backpropagation. The effect of Na_V separation is much smaller here than for the backpropagation threshold. The lines have been drawn to guide the eye.

3.2.4 Shift-Clamping the AIS

Na_V subtypes are defined by their gating properties. Each Na_V distribution (Figure 1) produces a corresponding spatial profile of gating properties, including *right-shift*. In Figure 6 we unravel the effects of Na_V separation on the backpropagation threshold in terms of the resulting spatial distribution of Na_V *right-shift* associated with $Na_V1.2$.

Our model sets the nominal *right-shift* of $Na_V1.2$ at $V_{RS} = 13.0\mathrm{mV}$, for compatibility with Hu et al. (2009).[2] In Figure 6 the AIS Na_V distribution is fixed at $x = 1$ (and $\kappa = 0.7$). This natural spatial separation of Na_Vs concentrates *right-shift* in the proximal AIS, by concentrating $Na_V1.2$ in that region

[2]Gating properties are detailed in Supporting Information, see Figure S7.

(see Figure 1). We use the parameter ΔV_{RS} to alter, in the AIS only, the *right-shift* of certain $\mathrm{Na_V1.2}$ properties; $\Delta V_{\mathrm{RS}} = 0$ for the nominal $\mathrm{Na_V1.2}$ properties.

Activation $m^{\mathrm{Na_V1.2}}$ and *availability* $h^{\mathrm{Na_V1.2}}$ are *right-shift*ed by similar amounts relative to their $\mathrm{Na_V1.6}$ counterparts Rush et al. (2005); Hu et al. (2009); Kole et al. (2008); Wang et al. (2009). (Although, certain receptors can temporarily *right-shift activation* without shifting steady-state *availability* Yin et al. (2015).) Altering this synchronous *right-shift* produces the reference curves in Figure 6a and Figure 6b, wherein ΔV_{RS} shifts every $\mathrm{Na_V1.2}$ gating property. That is, as functions of membrane potential, the steady-states and time constants are $m_\infty^{\mathrm{Na_V1.2}} = m_\infty^{\mathrm{Na_V1.2}}(V-\Delta V_{\mathrm{RS}})$, $\tau_m^{\mathrm{Na_V1.2}} = \tau_m^{\mathrm{Na_V1.2}}(V-\Delta V_{\mathrm{RS}})$, $h_\infty^{\mathrm{Na_V1.2}} = h_\infty^{\mathrm{Na_V1.2}}(V-\Delta V_{\mathrm{RS}})$, $\tau_h^{\mathrm{Na_V1.2}} = \tau_h^{\mathrm{Na_V1.2}}(V - \Delta V_{\mathrm{RS}})$ in the AIS.

Because ΔV_{RS} alters the spatially distributed gating properties in a way that is analogous to changing the $\mathrm{Na_V}$ distribution, Figure 6 connects gating properties to the results in Figure 4 and Figure 2. The reference curves confirm that proximal *right-shift* from $\mathrm{Na_V1.2}$ lowers the backpropagation threshold for axonal stimulation (Figure 6a) and *right-shift* raises Q_{BP} for somatic stimulation (Figure 6b). Restricting ΔV_{RS} to $\mathrm{Na_V1.2}$ within the AIS demonstrates that *right-shift*ed gating properties within the AIS alone are sufficient to explain the effects of $\mathrm{Na_V}$ distribution on the backpropagation threshold shown above.

Further in Figure 6, we "shift-clamp" selected gating properties: Ignoring the experimental and biophysical reality that $\mathrm{Na_V}$ *activation* and *availability* tend to *right-shift* in unison Rush et al. (2005); Wang et al. (2009); Boucher et al. (2012) and that gating variables and their voltage-sensitive time constants *right-shift* together as well Hodgkin and Huxley (1952), we probe causality in the model by

1. applying ΔV_{RS} to $h^{\mathrm{Na_V1.2}}$ independently of $m^{\mathrm{Na_V1.2}}$,
2. applying ΔV_{RS} to $\tau_h^{\mathrm{Na_V1.2}}(V)$ independently of $h_\infty^{\mathrm{Na_V1.2}}(V)$, and likewise for $\tau_m^{\mathrm{Na_V1.2}}$, $m_\infty^{\mathrm{Na_V1.2}}$;

and compute the new backpropagation threshold $Q_{BP}(\Delta V_{\mathrm{RS}})$. (For mathematical details see Section S1.1.) An example of the latter is Equation 1 below, in which only $\tau_h^{\mathrm{Na_V1.2}}$ has its *right-shift* modified by ΔV_{RS}. The other three properties have the nominal *right-shift* of $13\mathrm{mV}$. The $Q_{BP}(\Delta V_{\mathrm{RS}})$ curves in Figure 6 that

correspond to Equation 1 are legended ■ $\tau_h^{\mathrm{Na_V1.2}}$:

$$\text{“}\blacksquare\,\tau_h^{\mathrm{Na_V1.2}}\text{”} \longleftarrow \begin{cases} \tau_h^{\mathrm{Na_V1.2}} = \tau_h^{\mathrm{Na_V1.2}}(V - \Delta V_{\mathrm{RS}}) \\ h_\infty^{\mathrm{Na_V1.2}} = h_\infty^{\mathrm{Na_V1.2}}(V) \\ \tau_m^{\mathrm{Na_V1.2}} = \tau_m^{\mathrm{Na_V1.2}}(V) \\ m_\infty^{\mathrm{Na_V1.2}} = m_\infty^{\mathrm{Na_V1.2}}(V). \end{cases} \tag{1}$$

(Figure S8 visualizes the impact of Equation 1 on gating properties as a function of position at V_{rest}.)

To unpack Figure 6 we start at $\Delta V_{\mathrm{RS}} = 0$: the 'nominal point'. All curves in Figure 6a and Figure 6b intersect at the nominal point because $\mathrm{Na_V1.2}$ *right-shift* is nominal there for all gating properties. Starting at the nominal point, as one moves leftward along a given curve ($\Delta V_{\mathrm{RS}} < 0$), *right-shift* is removed from the gating properties indicated in the legend only.

With axonal stimulation the *right-shift* of *availability* drives $Q_{BP}(\Delta V_{\mathrm{RS}})$. Figure 6a reveals that the *right-shift*ed $h_\infty^{\mathrm{Na_V1.2}}$ and $\tau_h^{\mathrm{Na_V1.2}}$ work together to promote backpropagation (✚ $h_\infty^{\mathrm{Na_V1.2}} \cdot \tau_h^{\mathrm{Na_V1.2}}$), overpowering the threshold-raising influence of *activation right-shift* (▼ $m_\infty^{\mathrm{Na_V1.2}} \cdot \tau_m^{\mathrm{Na_V1.2}}$). Further, removing the *right-shift* of $\tau_h^{\mathrm{Na_V1.2}}$ stops backpropagation: in the ■ $\tau_h^{\mathrm{Na_V1.2}}$ curve, all other gating properties, including $h_\infty^{\mathrm{Na_V1.2}}$, retain their nominal *right-shift*, yet backpropagation ceases when $\Delta V_{\mathrm{RS}} \lesssim -2\mathrm{mV}$.

For somatic stimulation (Figure 6b) the *right-shift* of *activation* drives $Q_{BP}(\Delta V_{\mathrm{RS}})$. The greatest decrease in threshold occurs in the ▲ $m_\infty^{\mathrm{Na_V1.2}}$ and ▼ $m_\infty^{\mathrm{Na_V1.2}} \cdot \tau_m^{\mathrm{Na_V1.2}}$ curves as the nominal *right-shift* is removed ($\Delta V_{\mathrm{RS}} \longrightarrow -13.0\mathrm{mV}$). The ▼ $m_\infty^{\mathrm{Na_V1.2}} \cdot \tau_m^{\mathrm{Na_V1.2}}$ curve differs negligibly from the ▲ $m_\infty^{\mathrm{Na_V1.2}}$ curve, showing that $m_\infty^{\mathrm{Na_V1.2}}$ *right-shift* dominates in raising the threshold near the nominal point, and $\tau_m^{\mathrm{Na_V1.2}}$ matters little. Our ΔV_{RS} results are summarized in Table 1.

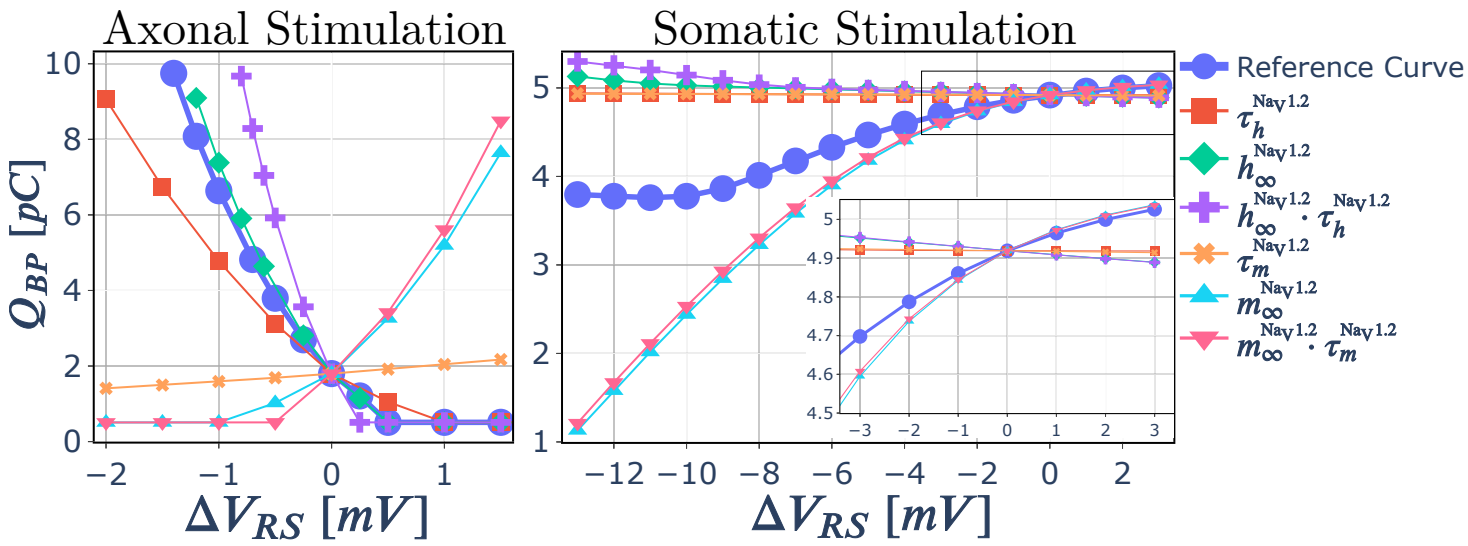

(a) (b)

Figure 6: Shift-Clamping selected gating properties reveals competing effects of $Na_V1.2$ *right-shift* on the backpropagation threshold. In the AIS, ΔV_{RS} modifies the *right-shift* of $Na_V1.2$ gating properties indicated in the legend. The reference curve (legended ●) shows the net effect of *right-shift* on $Q_{BP}(\Delta V_{RS})$ via its slope. Points on this curve are pulled toward all of the other shift-clamped curves, but to varying degrees. Comparing each curve to its respective reference curve reveals the key gating properties through which *right-shift* controls backpropagation for each type of stimulation. (a) Axonal stimulation: The reference curve has negative slope (*right-shift* lowers Q_{BP}), and tracks curves legended with $h_\infty^{Na_V1.2}$ or $\tau_h^{Na_V1.2}$. Backpropagation threshold is governed by proximal Na_V *availability*, owing to the *right-shift* of $Na_V1.2$, and is sensitive to its time constant. (b) Somatic stimulation: The reference curve has positive slope near the nominal point (*right-shift* raises Q_{BP}), and tracks curves legended with $m_\infty^{Na_V1.2}$ near the natural value of V_{RS} ($\Delta V_{RS} \longrightarrow 0$, see inset). Backpropagation threshold is governed by Na_V steady-state *activation* and is insensitive to all time constants. The lines have been drawn to guide the eye. In both plots $x = 1.0$ and $\kappa = 0.7$. Results are summarized in Table 1.

Table 1: Summary of Figure 6: Dissecting the impact of AIS $Na_V1.2$ *right-shift* on backpropagation threshold using shift-clamping

Type of Stimulation	reference curve	Increasing ΔV_{RS} of ***availability***		
		$\tau_h^{Na_V1.2}$	$h_\infty^{Na_V1.2}$	$h_\infty^{Na_V1.2} \cdot \tau_h^{Na_V1.2}$
Axonal	↓	↓	↓	↓
Somatic	↑	×	↓	↓
		Increasing ΔV_{RS} of ***activation***		
		$\tau_m^{Na_V1.2}$	$m_\infty^{Na_V1.2}$	$m_\infty^{Na_V1.2} \cdot \tau_m^{Na_V1.2}$
Axonal	↓	↑ (slight)	↑	↑
Somatic	↑	×	↑	↑

Arrows (↓,↑) summarize the sign of the slopes of backpropagation threshold curves in Figure 6a (axonal stimulation) and Figure 6b (somatic stimulation). A downward arrow (↓) indicates that the backpropagation threshold Q_{BP} decreases with increasing *right-shift*, applied to the kinetic variable(s) specified above it. Likewise, an upward arrow (↑) indicates an increased threshold when that combination of $Na_V1.2$ variables is *right-shift*ed. In cells marked "×" the effect of *right-shift* was negligible.

3.3 Discussion

Our results for antidromic stimulation (axonal current injection) agree qualitatively with and expand upon past modeling efforts Hu et al. (2009). The agreement is thorough since we show that both $\mathrm{Na_V}$ separation 'x-distribution' and distal translation of the crossover location κ promote backpropagation. That is, proximal accumulation of $\mathrm{Na_V}1.2$ lowers the threshold for backpropagation and further, increasing the total proportion of $\mathrm{Na_V}1.2$ in the AIS —by moving the $\mathrm{Na_V}$ crossover distally— promotes backpropagation as well. We also find that increased distal $\mathrm{Na_V}1.6$ concentration (which results from the natural distribution) lowers the AP threshold (Figure 5).

Although *right-shift*ing $\mathrm{Na_V}1.2$ steady-state *availability* $h_\infty^{\mathrm{Na_V}1.2}(V)$ is necessary to promote backpropagation, it is not sufficient on its own: our modelling shows that the voltage-sensitive time constant $\tau_h^{\mathrm{Na_V}1.2}(V)$ must be *right-shift*ed as well (Figure 6a). *Right-shift*ing steady-state $\mathrm{Na_V}1.2$ *availability alone* ($\blacklozenge\, h_\infty^{\mathrm{Na_V}1.2}$) increases Na^+ conductance at all voltages, as $h_\infty^{\mathrm{Na_V}1.2}(V)$ is monotonically decreasing. It is clear then why ΔV_{RS} lowers the threshold in the $\blacklozenge\, h_\infty^{\mathrm{Na_V}1.2}$ curves of Figure 6a and Figure 6b. However, it is far from obvious that removing the nominal *right-shift* of voltage-sensitive time constants, without modifying steady-state *activation* or *availability*, should on its own be sufficient to eliminate the backpropagation threshold-lowering effects of $\mathrm{Na_V}1.2$ for axonal stimulation. But that is what our model has demonstrated in the curve legended $\blacksquare\, \tau_h^{\mathrm{Na_V}1.2}$ in Figure 6a. It follows that the x-distribution's tendency to promote backpropagation is not merely a result of increased steady-state *availability* of proximal AIS $\mathrm{Na_V}$s, but is a dynamic effect —dependent on the intrinsic *right-shift* of $\tau_h^{\mathrm{Na_V}1.2}(V)$.

There is an interplay between cable properties and the distribution of $\mathrm{Na_V}$s in determining the site of AP initiation Ma and Huguenard (2013). Electrical isolation of the initiation site may amplify the effect of concentrating $\mathrm{Na_V}1.6$ in the distal AIS. Via fluorescence imaging of intracellular Na^+ concentration following single action potentials, Baranauskas et al. Baranauskas et al. (2013) located the greatest Na^+ influx at the middle of the AIS, whereas the distal AIS (initiation site) had only $1/4$ of this maximum. They inferred that the density of $\mathrm{Na_V}$ channels decreases toward the initiation site and thus $\mathrm{Na_V}$ density does not determine the precise location where APs begin. Although Baranauskas et al. (2013) did not require $\mathrm{Na_V}1.6$ accumulation at the distal AIS to explain the distal location of the initiation site, they suggest that local $\mathrm{Na_V}$ density can have a large effect on neuronal excitability. Temperature may also play a role in such local AIS Na^+ influx measurements due to the spatial separation of $\mathrm{Na_V}$ subtypes. To

reduce diffusion-blurring for highspeed sodium imaging they cooled their pyramidal neurons to 21℃. Ye et al.Ye et al. (2018) have shown that Na_V subtypes respond differently to temperature changes (see Fig. 8(H) of Ye et al. (2018)); thus a deeper exploration of the effects of temperature changes is warranted.

The qualitative dependence of the backpropagation threshold on the somatic-versus-axonal mode of stimulation is compatible with distal AP generation as found in Baranauskas et al. (2013); Hu et al. (2009) and in our work, but does not seem to rely crucially on the precise determinants of AP onset position; it relies rather on the activation and availability properties, and the kinetics of the latter.

Our results for orthodromic stimulation (somatic current injection) suggest that the cell is made less excitable by the proximal accumulation of $Na_V1.2$ which is characteristic of the χ-distribution. Depending on the crossover location κ, the parameter χ can either increase or decrease the backpropagation threshold along a constant κ curve (Figure 2). The threshold-raising effect of proximal $Na_V1.2$ is further confirmed by repeating the simulation procedure with a model cell in which the AIS has been flipped longitudinally (Figure 3), placing $Na_V1.6$ proximally and $Na_V1.2$ distally in the AIS. Our modeling indicates that the effects of the observed Na_V distribution depend on whether stimulation is orthodromic (e.g. somatodendritic input) or antidromic (e.g. axo-axonic input from interneurons).

Paradoxical hyperexcitability upon removal of $Na_V1.2$ has recently been reported and explained via reduced K_V *activation* as a secondary effect of reduced spike amplitude. Researching genetic causes of autism spectrum disorder Spratt et al. (2021) showed that $Na_V1.2$ knockout can enhance pyramidal cells' tendency to send action potentials and simultaneously reduce backpropagation (somatodendritic hypoexcitability). Our modeling shows a compatible result with a different explanation: reduced excitability owing to AIS $Na_V1.2$, explained by an asymmetry in the role of Na_V kinetics in the AIS with respect to axonal versus somatic stimulation. Whereas Spratt et al. (2021) reported an interplay between cellular $Na_V1.2$ and K_V, our results are explained by the distribution of Na_V *right-shift* within the AIS (Table 1, Figure 6b).

In summary, we have simulated a range of hypothetical Na_V distributions in the axon initial segment of a 3D-reconstructed biophysical pyramidal cell model. Our modeling shows that the spatial profile of $Na_V1.2$ and $Na_V1.6$ in the AIS and the kinetics of their *availability* and *activation* are important determinants of excitability and the backpropagation threshold. We predict that the observed separation of Na_V subtypes will have asymmetrical effects on excitability depending on whether the neuron is stimulated

orthodromically or antidromically. With orthodromic stimulation, Na_V separation impedes backpropagation and reduces excitability unless the crossover is brought close to the soma. Backpropagation and excitability are both enhanced by Na_V separation when stimulation is antidromic. Maintaining a static Na_V distribution, we altered the *right-shift* of selected $Na_V1.2$ gating properties. This revealed that steady-state *activation right-shift* controls the orthodromic backpropagation threshold, and dynamic *availability right-shift* is needed to fully explain the antidromic threshold slope. The model cell was kept identical in all results presented above; only the AIS was altered. Our results therefore can only be explained by the distribution of Na_V subtypes and Na_V *right-shift* within the AIS. Given the time-dependence of the antidromic threshold and the differential temperature sensitivity of $Na_V1.2$ versus $Na_V1.6$ Ye et al. (2018), there is good reason to expect that the effects of Na_V separation reported here will be temperature-dependent.

3.4 Materials and methods

We simulate a Layer 5 pyramidal neuron from cat visual cortex, modified from Mainen and Sejnowski (1996) (see SI, Section S1.2). The multicompartmental pyramidal cell model was implemented in NEURON 8.0 Carnevale and Hines (2006). Every compartment has explicit intracellular and extracellular concentrations of sodium, potassium, and chloride ions. The Nernst potentials E_{Na^+}, E_{K^+}, E_{Cl^-} are calculated locally from each compartment's specific ionic concentrations, which respond to transmembrane currents. Transmembrane concentration gradients of Na^+ and K^+ are maintained via active transport (Na^+/K^+-pump), and all ions are subject to longitudinal diffusion, both intra- and extracellular, implemented using NEURON's RxD facility McDougal et al. (2013). The cell maintains a resting potential $V_{rest} \cong -70\mathrm{mV}$ at steady-state, and restores this state following stimulation.

In past modeling, there is sometimes a long section of bare axon following the AIS, or myelination may begin immediately at the end of the AIS. To ensure our results did not depend on this morphological feature, we ran simulations (axonal and somatic stimulation) with and without a $400\mu\mathrm{m}$ section of bare axon separating the AIS from the first internode. The effects of Na_V distribution, summarized in Figures 2 and 4, were qualitatively identical and similar in magnitude with and without the bare axon.

4 Acknowledgments and funding sources

We acknowledge the support of the Natural Sciences and Engineering Research Council of Canada (NSERC). We wish to thank: Catherine E. Morris, for directing our attention to the AIS. Nicholas T. Carnevale and Robert A. McDougal, for generously helping us to solve a number of model implementation problems using NEURON. We also thank Louis Jacques for helpful discussion.

5 References

References

Ryota Adachi, Rei Yamada, and Hiroshi Kuba. Plasticity of the Axonal Trigger Zone. *Neuroscientist*, 21 (3):255–265, June 2015. ISSN 1073-8584. doi: 10.1177/1073858414535986. URL https://doi.org/10.1177/1073858414535986.

Gytis Baranauskas, Yaron David, and Ilya A. Fleidervish. Spatial mismatch between the Na+ flux and spike initiation in axon initial segment. *PNAS*, January 2013. ISSN 0027-8424, 1091-6490. doi: 10.1073/pnas.1215125110. URL https://www.pnas.org/content/early/2013/01/17/1215125110.

Pierre-Alexandre Boucher, Béla Joós, and Catherine E. Morris. Coupled left-shift of Nav channels: modeling the Na+-loading and dysfunctional excitability of damaged axons. *J Comput Neurosci*, 33(2): 301–319, October 2012. ISSN 1573-6873. doi: 10.1007/s10827-012-0387-7. URL https://doi.org/10.1007/s10827-012-0387-7.

Romain Brette. Sharpness of Spike Initiation in Neurons Explained by Compartmentalization. *PLOS Computational Biology*, 9(12):e1003338, December 2013. ISSN 1553-7358. doi: 10.1371/journal.pcbi.1003338. URL https://journals.plos.org/ploscompbiol/article?id=10.1371/journal.pcbi.1003338.

Nicholas T. Carnevale and Michael L. Hines. *The NEURON book*. Cambridge University Press, Cambridge, UK ; New York, 2006. ISBN 978-0-521-84321-8.

Dominique Debanne, Emilie Campanac, Andrzej Bialowas, Edmond Carlier, and Gisèle Alcaraz. Axon

Physiology. *Physiological Reviews*, 91(2):555–602, April 2011. ISSN 0031-9333. doi: 10.1152/physrev.00048.2009. URL https://journals.physiology.org/doi/full/10.1152/physrev.00048.2009.

Brent Doiron, André Longtin, Ray W. Turner, and Leonard Maler. Model of Gamma Frequency Burst Discharge Generated by Conditional Backpropagation. *Journal of Neurophysiology*, 86(4):1523–1545, October 2001. ISSN 0022-3077. doi: 10.1152/jn.2001.86.4.1523. URL https://journals.physiology.org/doi/full/10.1152/jn.2001.86.4.1523.

Allan T. Gulledge and Jaime J. Bravo. Neuron Morphology Influences Axon Initial Segment Plasticity. *eNeuro*, 3(1), January 2016. ISSN 2373-2822. doi: 10.1523/ENEURO.0085-15.2016. URL https://www.eneuro.org/content/3/1/ENEURO.0085-15.2016.

A. L. Hodgkin and A. F. Huxley. A quantitative description of membrane current and its application to conduction and excitation in nerve. *The Journal of Physiology*, 117(4):500–544, 1952. ISSN 1469-7793. doi: 10.1113/jphysiol.1952.sp004764. URL https://onlinelibrary.wiley.com/doi/abs/10.1113/jphysiol.1952.sp004764.

Wenqin Hu and Yousheng Shu. Axonal bleb recording. *Neurosci. Bull.*, 28(4):342–350, August 2012. ISSN 1995-8218. doi: 10.1007/s12264-012-1247-1. URL https://link.springer.com/article/10.1007/s12264-012-1247-1.

Wenqin Hu, Cuiping Tian, Tun Li, Mingpo Yang, Han Hou, and Yousheng Shu. Distinct contributions of Nav1.6 and Nav1.2 in action potential initiation and backpropagation. *Nat Neurosci*, 12(8):996–1002, August 2009. ISSN 1546-1726. doi: 10.1038/nn.2359. URL https://www.nature.com/articles/nn.2359.

Felix Höfflin, Alexander Jack, Christian Riedel, Julia Mack-Bucher, Johannes Roos, Corinna Corcelli, Christian Schultz, Petra Wahle, and Maren Engelhardt. Heterogeneity of the Axon Initial Segment in Interneurons and Pyramidal Cells of Rodent Visual Cortex. *Frontiers in Cellular Neuroscience*, 11:332, 2017. ISSN 1662-5102. doi: 10.3389/fncel.2017.00332. URL https://www.frontiersin.org/article/10.3389/fncel.2017.00332.

Efrat Katz, Ohad Stoler, Anja Scheller, Yana Khrapunsky, Sandra Goebbels, Frank Kirchhoff, Michael J.

Gutnick, Fred Wolf, and Ilya A. Fleidervish. Role of sodium channel subtype in action potential generation by neocortical pyramidal neurons. *PNAS*, 115(30):E7184–E7192, July 2018. ISSN 0027-8424, 1091-6490. doi: 10.1073/pnas.1720493115. URL https://www.pnas.org/content/115/30/E7184.

Maarten H. P. Kole and Greg J. Stuart. Signal Processing in the Axon Initial Segment. *Neuron*, 73 (2):235–247, January 2012. ISSN 0896-6273. doi: 10.1016/j.neuron.2012.01.007. URL https://www.sciencedirect.com/science/article/pii/S0896627312000505.

Maarten H. P. Kole, Susanne U. Ilschner, Björn M. Kampa, Stephen R. Williams, Peter C. Ruben, and Greg J. Stuart. Action potential generation requires a high sodium channel density in the axon initial segment. *Nat Neurosci*, 11(2):178–186, February 2008. ISSN 1546-1726. doi: 10.1038/nn2040. URL https://www.nature.com/articles/nn2040.

Yunyong Ma and John R. Huguenard. Reemerging role of cable properties in action potential initiation. *PNAS*, 110(10):3715–3716, March 2013. ISSN 0027-8424, 1091-6490. doi: 10.1073/pnas.1300520110. URL https://www.pnas.org/content/110/10/3715.

Zachary F. Mainen and Terrence J. Sejnowski. Influence of dendritic structure on firing pattern in model neocortical neurons. *Nature*, 382(6589):363–366, July 1996. ISSN 1476-4687. doi: 10.1038/382363a0. URL https://www.nature.com/articles/382363a0.

Zachary F. Mainen, Jasdan Joerges, John R. Huguenard, and Terrence J. Sejnowski. A model of spike initiation in neocortical pyramidal neurons. *Neuron*, 15(6):1427–1439, December 1995. ISSN 0896-6273. doi: 10.1016/0896-6273(95)90020-9. URL https://www.sciencedirect.com/science/article/pii/0896627395900209.

Robert A. McDougal, Michael L. Hines, and William W. Lytton. Reaction-diffusion in the NEURON simulator. *Front. Neuroinform.*, 7, 2013. ISSN 1662-5196. doi: 10.3389/fninf.2013.00028. URL http://journal.frontiersin.org/article/10.3389/fninf.2013.00028/abstract.

Alexandre Payeur, Jordan Guerguiev, Friedemann Zenke, Blake A. Richards, and Richard Naud. Burst-dependent synaptic plasticity can coordinate learning in hierarchical circuits. *Nat Neurosci*, 24(7): 1010–1019, July 2021. ISSN 1546-1726. doi: 10.1038/s41593-021-00857-x. URL https://www.nature.com/articles/s41593-021-00857-x.

Anders Victor Petersen, Florence Cotel, and Jean-François Perrier. Plasticity of the Axon Initial Segment: Fast and Slow Processes with Multiple Functional Roles. *Neuroscientist*, 23(4):364–373, August 2017. ISSN 1073-8584. doi: 10.1177/1073858416648311. URL https://doi.org/10.1177/1073858416648311.

Wade G. Regehr, Megan R. Carey, and Aaron R. Best. Activity-Dependent Regulation of Synapses by Retrograde Messengers. *Neuron*, 63(2):154–170, July 2009. ISSN 0896-6273. doi: 10.1016/j.neuron.2009.06.021. URL https://www.sciencedirect.com/science/article/pii/S0896627309005078.

Anthony M. Rush, Sulayman D. Dib-Hajj, and Stephen G. Waxman. Electrophysiological properties of two axonal sodium channels, Na $_{v}$ 1.2 and Na $_{v}$ 1.6, expressed in mouse spinal sensory neurones: Sodium channels in sensory neurones. *The Journal of Physiology*, 564(3):803–815, May 2005. ISSN 00223751. doi: 10.1113/jphysiol.2005.083089. URL https://onlinelibrary.wiley.com/doi/10.1113/jphysiol.2005.083089.

E. Samson, J. Marchand, and K. A. Snyder. Calculation of ionic diffusion coefficients on the basis of migration test results. *Mat. Struct.*, 36(3):156–165, April 2003. ISSN 1871-6873. doi: 10.1007/BF02479554. URL https://link.springer.com/article/10.1007/BF02479554.

Gordon M. Shepherd, Luis Marenco, Michael L. Hines, Michele Migliore, Robert A. McDougal, Nicholas T. Carnevale, Adam J. H. Newton, Monique Surles-Zeigler, and Giorgio A. Ascoli. Neuron Names: A Gene- and Property-Based Name Format, With Special Reference to Cortical Neurons. *Frontiers in Neuroanatomy*, 13, 2019. ISSN 1662-5129. URL https://www.frontiersin.org/article/10.3389/fnana.2019.00025.

Perry W. E. Spratt, Ryan P. D. Alexander, Roy Ben-Shalom, Atehsa Sahagun, Henry Kyoung, Caroline M. Keeshen, Stephan J. Sanders, and Kevin J. Bender. Paradoxical hyperexcitability from NaV1.2 sodium channel loss in neocortical pyramidal cells. *Cell Reports*, 36(5), August 2021. ISSN 2211-1247. doi: 10.1016/j.celrep.2021.109483. URL https://www.cell.com/cell-reports/abstract/S2211-1247(21)00910-4.

Cuiping Tian, Kaiyan Wang, Wei Ke, Hui Guo, and Yousheng Shu. Molecular identity of axonal sodium channels in human cortical pyramidal cells. *Front. Cell. Neurosci.*, 8, September 2014. ISSN 1662-

5102. doi: 10.3389/fncel.2014.00297. URL http://journal.frontiersin.org/article/10.3389/fncel.2014.00297/abstract.

Christophe Verbist, Michael G. Müller, Huibert D. Mansvelder, Robert Legenstein, and Michele Giugliano. The location of the axon initial segment affects the bandwidth of spike initiation dynamics. *PLOS Computational Biology*, 16(7):e1008087, July 2020. ISSN 1553-7358. doi: 10.1371/journal.pcbi.1008087. URL https://journals.plos.org/ploscompbiol/article?id=10.1371/journal.pcbi.1008087.

Zvonimir Vrselja, Stefano G. Daniele, John Silbereis, Francesca Talpo, Yury M. Morozov, André M. M. Sousa, Brian S. Tanaka, Mario Skarica, Mihovil Pletikos, Navjot Kaur, Zhen W. Zhuang, Zhao Liu, Rafeed Alkawadri, Albert J. Sinusas, Stephen R. Latham, Stephen G. Waxman, and Nenad Sestan. Restoration of brain circulation and cellular functions hours post-mortem. *Nature*, 568(7752):336–343, April 2019. ISSN 1476-4687. doi: 10.1038/s41586-019-1099-1. URL https://www.nature.com/articles/s41586-019-1099-1.

Jun A. Wang, Wei Lin, Terence Morris, Umberto Banderali, Peter F. Juranka, and Catherine E. Morris. Membrane trauma and Na+ leak from Nav1.6 channels. *American Journal of Physiology-Cell Physiology*, 297(4):C823–C834, October 2009. ISSN 0363-6143. doi: 10.1152/ajpcell.00505.2008. URL https://journals.physiology.org/doi/full/10.1152/ajpcell.00505.2008.

Mingyu Ye, Jun Yang, Cuiping Tian, Qiyu Zhu, Luping Yin, Shan Jiang, Mingpo Yang, and Yousheng Shu. Differential roles of NaV1.2 and NaV1.6 in regulating neuronal excitability at febrile temperature and distinct contributions to febrile seizures. *Sci Rep*, 8(1):753, December 2018. ISSN 2045-2322. doi: 10.1038/s41598-017-17344-8. URL http://www.nature.com/articles/s41598-017-17344-8.

Luping Yin, Malte J. Rasch, Quansheng He, Si Wu, Fei Dou, and Yousheng Shu. Selective Modulation of Axonal Sodium Channel Subtypes by 5-HT $_{1a}$ Receptor in Cortical Pyramidal Neuron. *Cereb. Cortex*, page bhv245, October 2015. ISSN 1047-3211, 1460-2199. doi: 10.1093/cercor/bhv245. URL https://academic.oup.com/cercor/article-lookup/doi/10.1093/cercor/bhv245.

6 Figure legends

Figure 1

Figure 1: Modifying the spatial distribution of Na_V subtypes in the AIS while keeping the total conductance constant. For visual clarity, we have lengthened the AIS to $50\mu m$. (a) The spatial separation of Na_V subtypes in the AIS is varied using the parameter "x" with $\kappa = 0.5$. The top plot is a model setup that mimics the observed distribution Hu et al. (2009) of Na_Vs in the AIS. The high threshold $Na_V1.2$ (indicated in blue) are concentrated close to the soma and the low threshold $Na_V1.6$ (indicated in orange) are kept distal to the soma. Moving from top to bottom, both Na_V subtypes are distributed ever more evenly along the AIS. We chose the parameter name "x" to vary the spatial separation of the AIS Na_V distributions because the natural distribution is x-shaped. Setting $x = 1$ in our simulations gives the natural distribution, and $x = 0$ gives the "flat" distribution wherein both Na_V subtypes are uniformly mixed. (b) Variation of the crossover location (κ) of Na_Vs in the AIS with $x = 0.5$.

Figure 2

Figure 2: Somatic Stimulation: Combined effect of varying crossover location (κ) and Na_V separation (x) in the axon initial segment. The threshold for forward AP propagation is the same as for backpropagation. Varying the separation parameter "x" from $x = 0$ to $x = 1$, the distribution of Na_V channels goes from flat (artificial) to separated, the latter approximating the distribution observed in nature (see Figure 1a). Note that curves for all values of κ converge to a single point at $x = 0$, since κ can have no effect when the two Na_V's are uniformly distributed along the AIS. The lines have been drawn to guide the eye.

Figure 3

Figure 3: When the AIS Na_V distribution is flipped, setting $x = 1$ concentrates $Na_V1.6$ at the proximal AIS and $Na_V1.2$ at the distal AIS —the opposite of what is observed in many pyramidal cells Hu et al. (2009); Tian et al. (2014); Ye et al. (2018). (a) AIS with natural longitudinal placement of Na_Vs. (b) AIS with longitudinally flipped Na_V distribution. In both plots $x = 0.5$ and $\kappa = 0.5$. (c) Somatic stimulation with AIS Na_Vs flipped as in (b): This result is close to a mirror image of Figure 2. The lines have been

drawn to guide the eye.

Figure 4

Figure 4: Axonal Stimulation: Effect of varying crossover location (κ) and $\mathrm{Na_V}$ separation (x) in the AIS on backpropagation threshold. Separating the two $\mathrm{Na_V}$ subtypes ($x \longrightarrow 1$) lowers the threshold, in agreement with Hu et al. (2009) who found that proximal accumulation of $\mathrm{Na_V}1.2$ promotes backpropagation, albeit due to different gating properties (Figure 6a). Increasing κ raises the proportion of $\mathrm{Na_V}1.2$ (relative to $\mathrm{Na_V}1.6$) in the AIS and lowers the backpropagation threshold as well. Threshold changes here are larger than for somatic stimulation (Figure 2). When computing the threshold at different values of x and κ, the stimulating current was limited to a maximum of $10\mathrm{nA}$. To achieve backpropagation within that constraint (following axonal stimulation), our model required some amount of proximal $\mathrm{Na_V}1.2$, delivered through the combined effects of $\mathrm{Na_V}$ separation ($x \gtrsim 0.5$) and a sufficiently distal crossover position $\kappa \gtrsim 0.4$. The lines have been drawn to guide the eye.

Figure 5

Figure 5: Axonal Stimulation: Effect of x and κ on forward propagation threshold. The trend for all constant κ curves is that a higher proportion of total AIS $\mathrm{Na_V}1.6$ or a higher density of distal AIS $\mathrm{Na_V}1.6$ lowers the threshold to initiate forward propagating action potentials. Note that this threshold is not sufficient to achieve backpropagation. The effect of $\mathrm{Na_V}$ separation is much smaller here than for the backpropagation threshold. The lines have been drawn to guide the eye.

Figure 6

Figure 6: Shift-Clamping selected gating properties reveals competing effects of $\mathrm{Na_V}1.2$ *right-shift* on the backpropagation threshold. In the AIS, ΔV_{RS} modifies the *right-shift* of $\mathrm{Na_V}1.2$ gating properties indicated in the legend. The reference curve (legended ●) shows the net effect of *right-shift* on $Q_{BP}(\Delta V_{\mathrm{RS}})$ via its slope. Points on this curve are pulled toward all of the other shift-clamped curves, but to varying degrees. Comparing each curve to its respective reference curve reveals the key gating properties through which *right-shift* controls backpropagation for each type of stimulation. (a) Axonal stimulation: The

reference curve has negative slope (*right-shift* lowers Q_{BP}), and tracks curves legended with $h_\infty^{\mathrm{Na_V1.2}}$ or $\tau_h^{\mathrm{Na_V1.2}}$. Backpropagation threshold is governed by proximal $\mathrm{Na_V}$ *availability*, owing to the *right-shift* of $\mathrm{Na_V}1.2$, and is sensitive to its time constant. (b) Somatic stimulation: The reference curve has positive slope near the nominal point (*right-shift* raises Q_{BP}), and tracks curves legended with $m_\infty^{\mathrm{Na_V1.2}}$ near the natural value of V_{RS} ($\Delta V_{\mathrm{RS}} \longrightarrow 0$, see inset). Backpropagation threshold is governed by $\mathrm{Na_V}$ steady-state *activation* and is insensitive to all time constants. The lines have been drawn to guide the eye. In both plots $x = 1.0$ and $\kappa = 0.7$. Results are summarized in Table 1.

Table 1

Table 1: Arrows (↓,↑) summarize the sign of the slopes of backpropagation threshold curves in Figure 6a (axonal stimulation) and Figure 6b (somatic stimulation). A downward arrow (↓) indicates that the backpropagation threshold Q_{BP} decreases with increasing *right-shift*, applied to the kinetic variable(s) specified above it. Likewise, an upward arrow (↑) indicates an increased threshold when that combination of $\mathrm{Na_V}1.2$ variables is *right-shift*ed. In cells marked "×" the effect of *right-shift* was negligible.

7 Supporting information (SI)

S1.1 Shift-Clamping and the Hodgkin-Huxley model

In the Hodgkin-Huxley model Hodgkin and Huxley (1952) a gating variable u evolves according to its voltage-dependent forward and backward transition rates $\alpha_u(V)$ and $\beta_u(V)$ as

$$\frac{du}{dt} = \alpha_u(V)\big[1-u\big] - \beta_u(V)u, \tag{S1}$$

where u could be $\mathrm{Na_V}$ *activation* m or *availability* h, or $\mathrm{K_V}$ *activation* n etc. This can be rewritten using the steady-state $u_\infty(V)$ and voltage-dependent time constant $\tau_u(V)$ of the gating variable

$$\frac{du}{dt} = \frac{u_\infty(V) - u}{\tau_u(V)}, \tag{S2}$$

where u_∞ and τ_u are computed from α_u and β_u via

$$u_\infty(V) = \frac{\alpha_u(V)}{\alpha_u(V)+\beta_u(V)} \quad \text{and} \quad \tau_u(V) = \frac{1}{\alpha_u(V)+\beta_u(V)} \quad . \tag{S3}$$

When shifting the voltage-dependence of u_∞ by ΔV_{RS}, it is natural to assume that one should apply the same shift to τ_u given Equation S3, since u_∞ and τ_u are both functions of $\alpha_u(V)$ and $\beta_u(V)$ in such models. However, our simulations can shift $u_\infty(V)$ or $\tau_u(V)$ independently of one another: e.g. $\tau'_u(V) = \tau_u(V - \Delta V_{\mathrm{RS}})$, $u'_\infty(V) = u_\infty(V)$. The forward and backward rates become

$$\alpha'_u = \frac{u'_\infty(V)}{\tau'_u(V)} \quad \text{and} \quad \beta'_u = \frac{1-u'_\infty(V)}{\tau'_u(V)}. \tag{S4}$$

Putting this to use, one can modify the *right-shift* of combinations of

$$\Big\{\tau_h^{\mathrm{Na_V1.2}}(V),\ h_\infty^{\mathrm{Na_V1.2}}(V),\ \tau_m^{\mathrm{Na_V1.2}}(V),\ m_\infty^{\mathrm{Na_V1.2}}(V)\Big\}, \tag{S5}$$

by adding "$-\Delta V_{\mathrm{RS}}$" to the argument of the selected variables' $u_\infty(V)$s or $\tau_u(V)$s.

S1.2 Model: pyramidal cell geometry

Figure S1 displays the neuron used in this paper. The dendritic morphology is a digital reconstruction of a Layer 5 pyramidal neuron from cat visual cortex, modified from Mainen and Sejnowski (1996). These neurons have dendrites roughly as tall as the thickness of the cortex (several mm) and axon initial segment length similar to the width of a human hair (tens of $\mu\mathrm{m}$ Kole and Stuart (2012)).

Figure S1: Geometry of the model cell: Layer 5 pyramidal neuron from cat visual cortex, modified from Mainen and Sejnowski (1996). Somatodendritic morphology is digitally reconstructed from a real cell; hillock, AIS, and axon are added. Image created using blenderNEURON: blenderNEURON.org, blender.org.

The same cell geometry was used in Hu et al. (2009) and Kole et al. (2008). A cylindrical axon morphologically similar to that used in Hu et al. (2009) was attached to the reconstructed soma by a $10\mu\mathrm{m}$ long tapered hillock. The axon proper includes fifteen nodes of Ranvier (pink dots on the axon in Figure S2) separated by myelinated $100\mu\mathrm{m}$ internodes. The axon initial segment length was set to $\ell = 25.0\mu\mathrm{m}$, consistent with Höfflin et al. (2017). Voltage-gated channels are present all over the cell. Channel densities and passive leaks are given as conductances. The local conductances vary with position —representative values have been tabulated in Section S1.9.

S1.3 Spikes and Backpropagation in the Model

When pyramidal cells spike, the action potential can travel backward into the dendrites. This phenomenon is called backpropagation. Figure S2 illustrates spikes with and without backpropagation. Peak voltage is recorded across the entire cell model. The peak voltage at the tips of the dendrites is indicated in orange

and has a higher amplitude consistent with the sealed-end effect. Backpropagation was deemed to have occurred when the mean peak voltage of dendritic tips exceeded $-10.0\mathrm{mV}$ following stimulation.

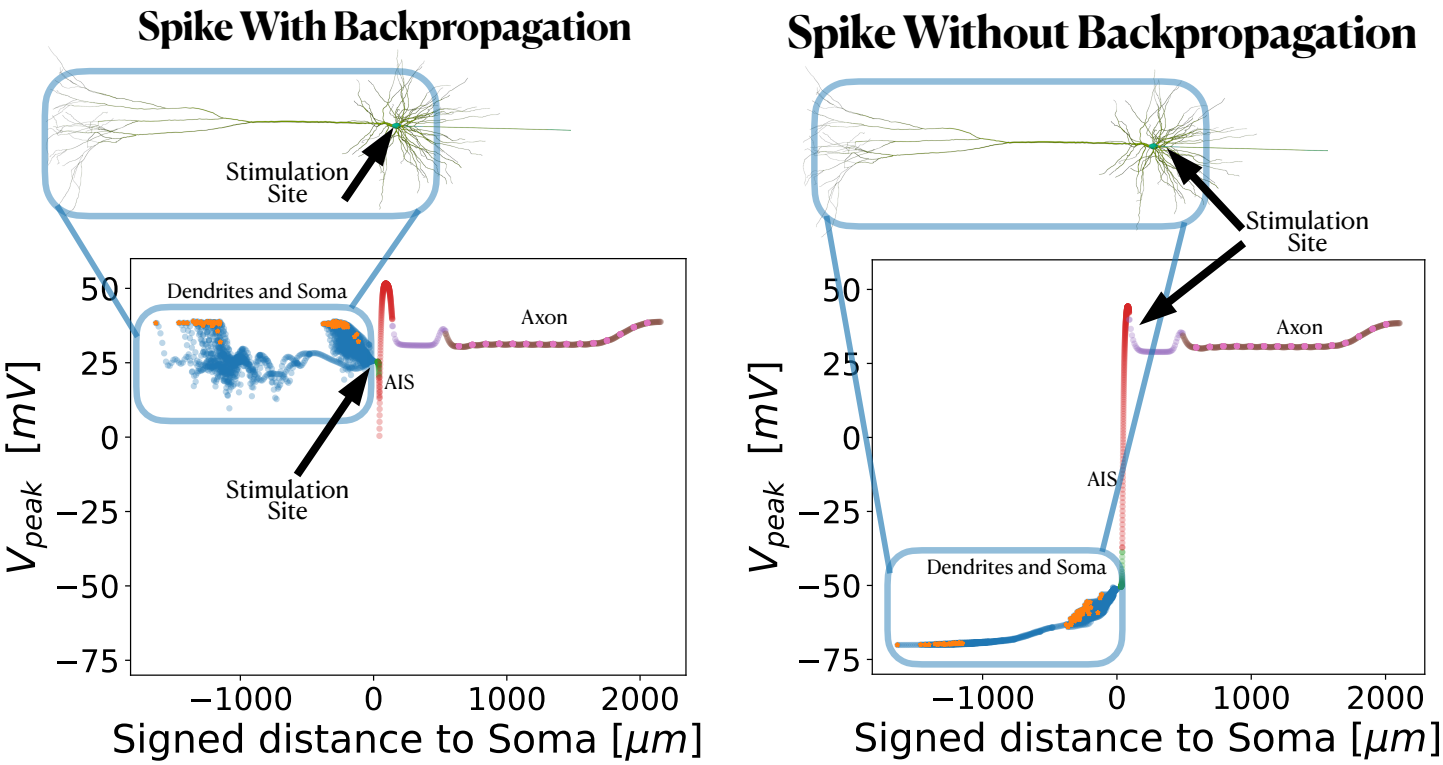

Figure S2: Spikes with and without backpropagation: Beginning on the right hand side: an action potential (AP) has occurred following axonal stimulation (current injected just distal to the AIS). Note that the peak voltage in the soma and dendrites remains near the resting potential $\approx -70\mathrm{mV}$, indicating that backpropagation did not occur. We call this scenario where an AP has been sent down the axon orthodromically from the stimulation site (i.e. to the right in this panel) without a somatodendritic spike "forward propagation" or "forwardprop". To the left is an AP that backpropagated: the entire cell spiked, in this case following somatic stimulation; backpropagation can occur following axonal stimulation as well. The somatodendritic peak voltages are indicated by a blue box in each case. This and similar figures are inspired by "Figure 4" of Mainen et al. (1995).

S1.4 Additional Simulations

Figure S3 demonstrates that increasing κ raises the backpropagation threshold when current is injected somatodendritically (orthodromic stimulation), even when the slopes in Figure 2 are negative. Increasing κ means moving the $\mathrm{Na_V}$ crossover location away from the soma, which increases the proportion of $\mathrm{Na_V}1.2$ (versus $\mathrm{Na_V}1.6$) in the AIS; see Figure 1b.

In the main text we found that with a $25\mu\mathrm{m}$ AIS, the slope of Q_{BP} versus x for somatic stimulation became flat around $\kappa \approx 0.4$ which is $20\mu\mathrm{m}$ away from the soma since $L_{\mathrm{hillock}} = 10\mu\mathrm{m}$ (Figure 2). In

Figure S4, with a **100μm** AIS the Q_{BP} slope flattens around $\kappa \approx 0.1$, which again corresponds to a distance of roughly **20μm** from the soma. This suggests that the threshold-lowering effect of Na_V separation for small κ (Figure 2) results from the increased proximal density of $Na_V1.6$ when the crossover is brought near to the soma —and is not due to the proximal density of $Na_V1.2$, consistent with Figure S3.

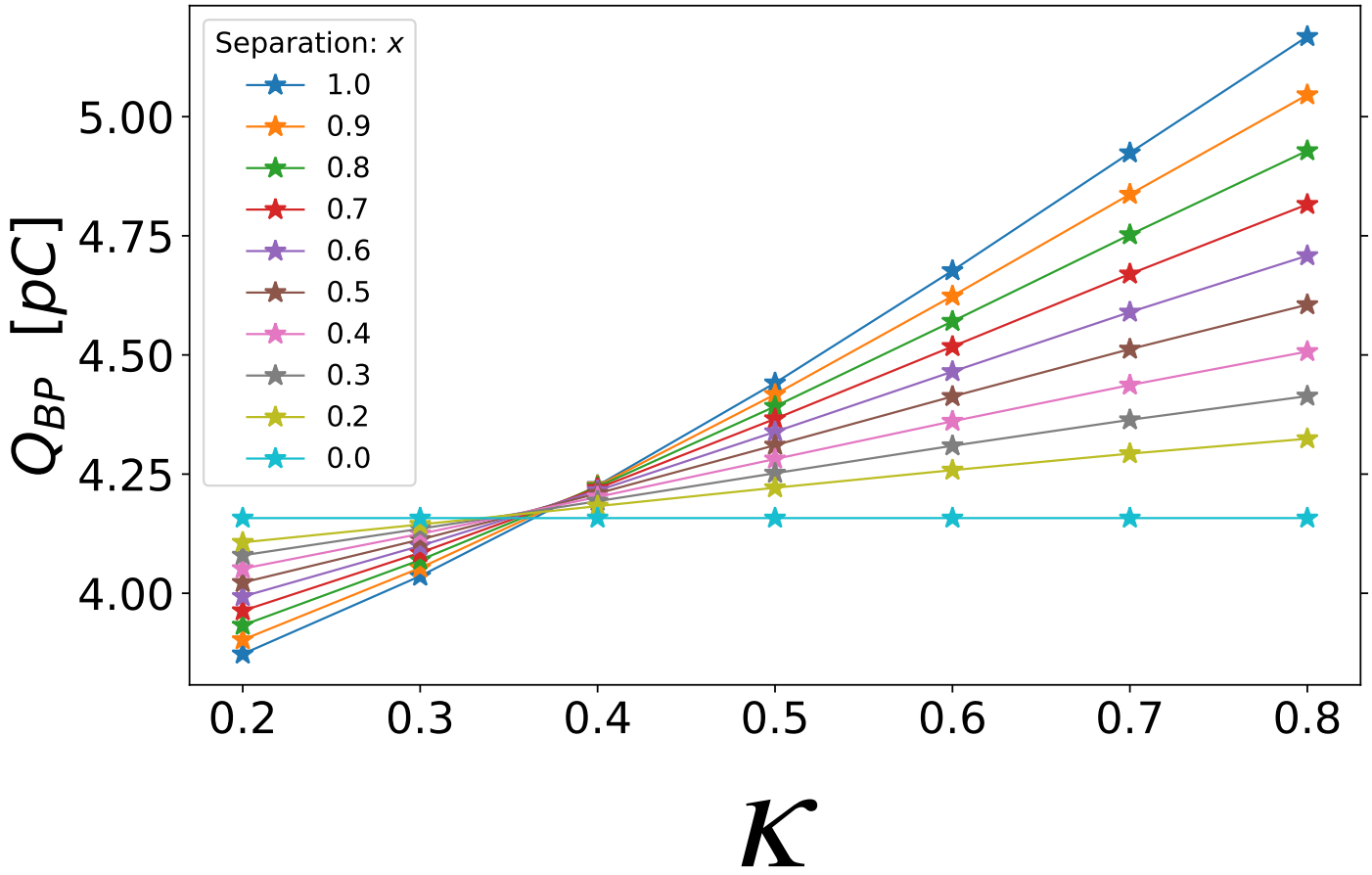

Figure S3: Somatic Stimulation: Combined effect of varying crossover location (κ) and Na_V separation (x) in the axon initial segment. Increasing κ raises the backpropagation threshold. Here the abscissa is normalized crossover position κ, instead of Na_V separation (compare with Figure 2). In Figure 2 all curves converge at $x = 0$. Here, that intersection point is replaced by the $x = 0$ *line*. Notice that every $x > 0$ curve has positive slope: the backpropagation threshold Q_{BP} *increases* with κ. Increasing κ when $x > 0$ necessarily increases the ratio of $Na_V1.2$ conductance to $Na_V1.6$ conductance in the AIS (see Equation S7). It follows that the natural separation of $Na_V1.2$ toward the proximal AIS raises the backpropagation threshold for somatic stimulation. The lines have been drawn to guide the eye.

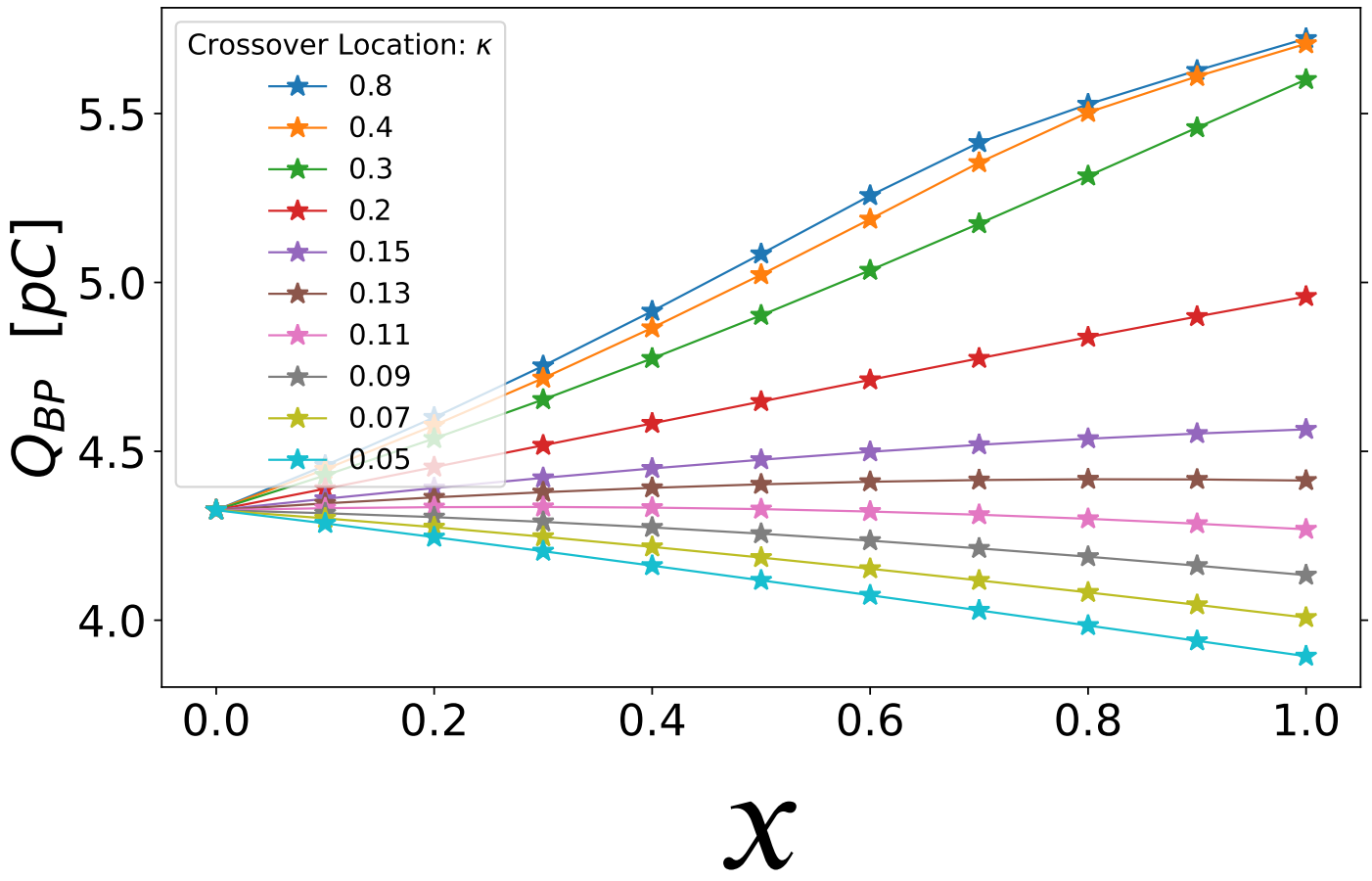

Figure S4: Somatic Stimulation with AIS lengthened to **100μm** (in the main text AIS length is **25μm**): Combined effect of varying crossover location (κ) and Na_V separation (x) in the axon initial segment. The lines have been drawn to guide the eye.

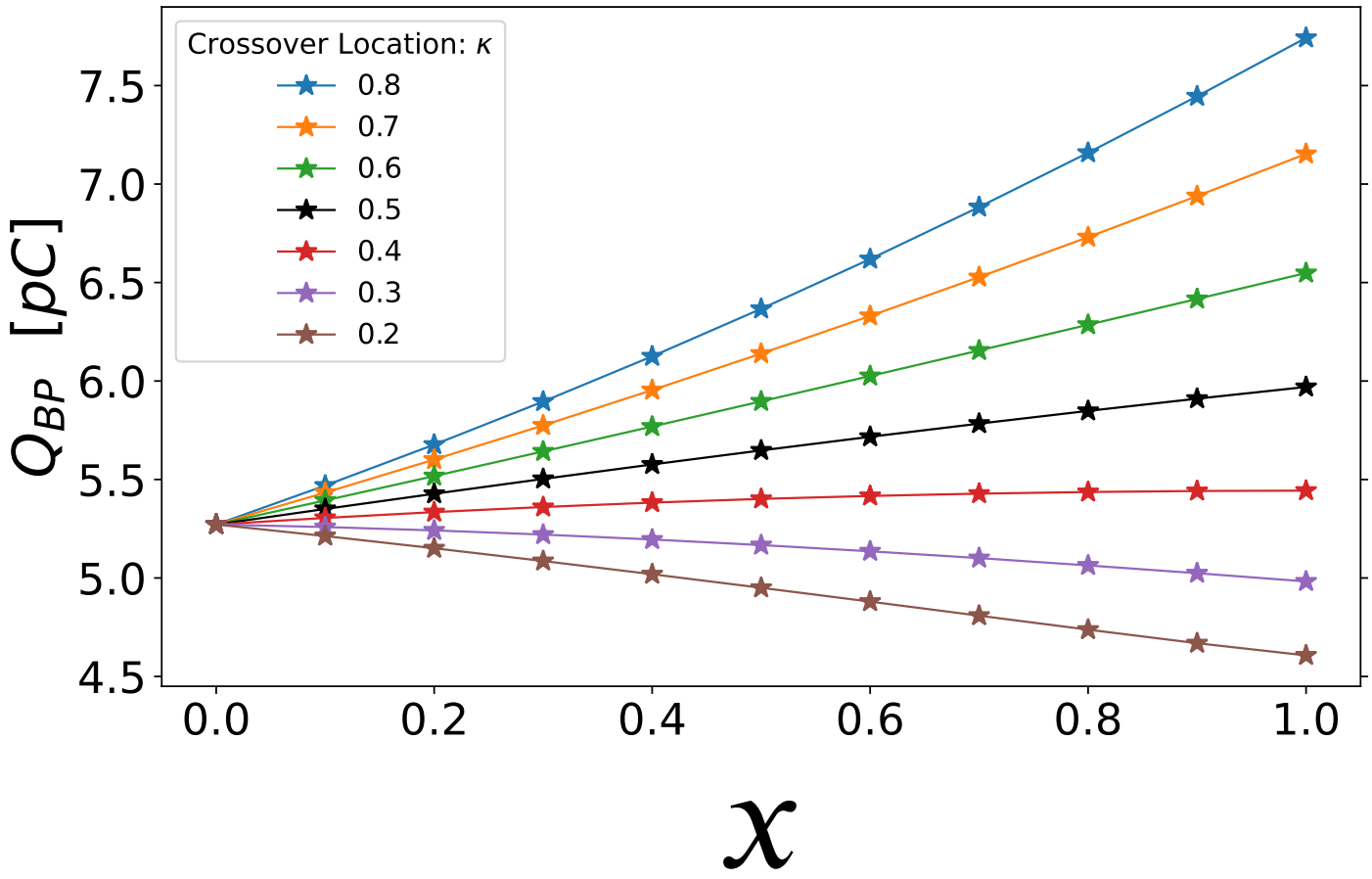

Figure S5: Dendritic Stimulation: current injection at the main apical dendrite yields the same qualitative behavior as for somatic stimulation. Compare with (Figure 2). Varying the separation parameter "x" from $x = 0$ to $x = 1$, the distribution of Na_V channels goes from flat (artificial) to separated, the latter approximating the distribution observed in nature (see Figure 1a). Note that curves for all values of κ converge to a single point at $x = 0$, since κ can have no effect when the two Na_V's are uniformly distributed along the AIS. The lines have been drawn to guide the eye.

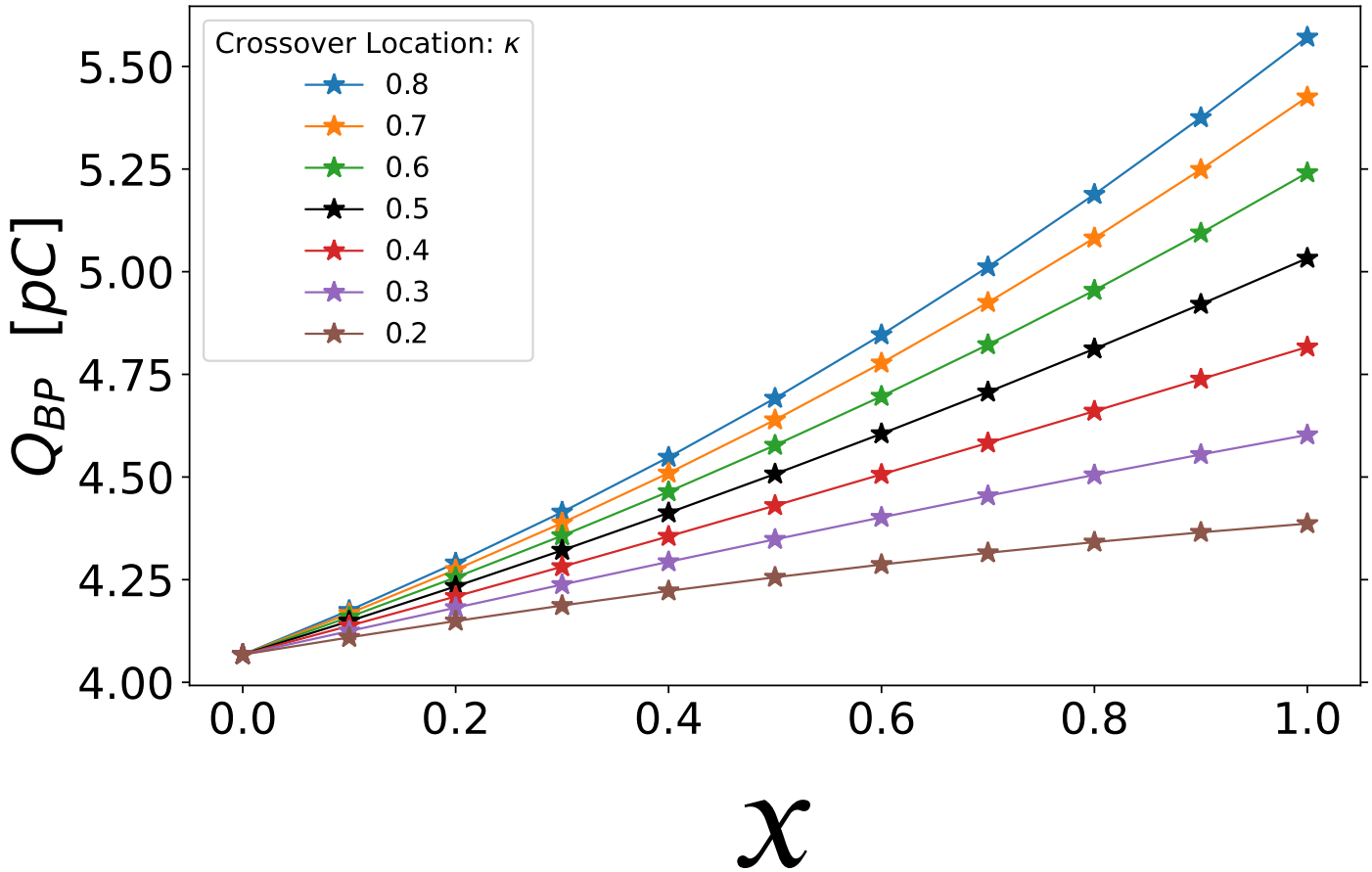

Figure S6: Somatic Stimulation: lengthening the hillock to $30\mu\mathbf{m}$ removes the negative slopes observed in Figure 2 and Figure S4. In all other plots we have used $L_{\text{hillock}} = 10\mu\mathbf{m}$. The lines have been drawn to guide the eye.

S1.5 AIS - technical details

In our model, the density profiles of $\text{Na}_\text{V}1.2$ and $\text{Na}_\text{V}1.6$ are left- and right-handed sigmoidal functions (respectively) of normalized length s along the AIS. The channel densities are expressed as maximal conductances $\bar{g}_{\text{Na}_\text{V}1.2}$ (s) and $\bar{g}_{\text{Na}_\text{V}1.6}$ (s):

$$\begin{cases} \bar{g}_{\text{Na}_\text{V}1.2}(s) &= \dfrac{\bar{g}_{\text{Na}_\text{V}}}{2}\Big(1 - x \cdot \tanh\big(\sigma(s-\kappa)\big)\Big), \\ \bar{g}_{\text{Na}_\text{V}1.6}(s) &= \bar{g}_{\text{Na}_\text{V}} - \bar{g}_{\text{Na}_\text{V}1.2}(s) \\ &= \dfrac{\bar{g}_{\text{Na}_\text{V}}}{2}\Big(1 + x \cdot \tanh\big(\sigma(s-\kappa)\big)\Big), \end{cases} \tag{S6}$$

where the total maximal $\mathrm{Na_V}$ conductance $\bar{g}_{\mathrm{Na_V}}$ is constant along the AIS:

$$\bar{g}_{\mathrm{Na_V}} = \bar{g}_{\mathrm{Na_V1.2}}(s) + \bar{g}_{\mathrm{Na_V1.6}}(s) = \boldsymbol{const.} \tag{S7}$$

We chose the hyperbolic tangent function $\tanh(s)$, but other sigmoidal functions would do just as well. The parameter x controls the separation of the $\mathrm{Na_V}$ distribution, that is, how separated the two $\mathrm{Na_V}$ subtypes are. When $x = 0$, the distribution becomes flat —$\mathrm{Na_V1.2}$ and $\mathrm{Na_V1.6}$ are mixed uniformly along the AIS. When $x = 1$, the proximal end of the AIS contains only $\mathrm{Na_V1.2}$, and the distal end of the AIS contains only $\mathrm{Na_V1.6}$. The parameter σ is the reciprocal of the 'transition width' of the AIS $\mathrm{Na_V}$ distributions normalized by the AIS length. In all simulations shown here, $\sigma = 0.1$.

The total $\mathrm{Na_V}$ conductance of the AIS is proportional to AIS length ℓ since its diameter is constant

$$\bar{G}_{\mathrm{Na_V}} = \bar{g}_{\mathrm{Na_V}} \cdot (\text{Area of AIS}) \propto \bar{g}_{\mathrm{Na_V}}\, \ell_{\mathrm{AIS}}. \tag{S8}$$

The contribution to this total conductance from $\mathrm{Na_V1.2}$ is

$$\bar{G}_{\mathrm{Na_V1.2}} \propto \int_0^{\ell_{\mathrm{AIS}}} d\ell'\, \bar{g}_{\mathrm{Na_V1.2}}(\ell') = \ell_{\mathrm{AIS}} \int_0^1 ds\, \frac{\bar{g}_{\mathrm{Na_V}}}{2}\Big(1 - x \cdot \tanh\big(\sigma(s-\kappa)\big)\Big), \tag{S9}$$

$$\Rightarrow \bar{G}_{\mathrm{Na_V1.2}} \propto 1 - x \cdot \underbrace{\left(\frac{\ln\big(\cosh(\sigma) - \sinh(\sigma)\tanh(\sigma\kappa)\big)}{\sigma}\right)}_{\text{“}M\text{”}}. \tag{S10}$$

The root of the term labelled "M" in Equation S10 is $\kappa = \frac{1}{2}$, and the slope of M is negative: $M(\kappa < 0.5) > 0$, $M(\kappa > 0.5) < 0$. Since $M(\kappa = 0.5) = 0$, the derivative of $\bar{G}_{\mathrm{Na_V1.2}}$ (and $\bar{G}_{\mathrm{Na_V1.6}}$) with respect to x is zero when the crossover is located in the middle of the AIS, which is the standard configuration for varying $\mathrm{Na_V}$ separation. We call $\kappa = 0.5$ standard because, in this configuration, the effects on the backpropagation threshold due to varying x can not be due to changes in the total conductance of $\mathrm{Na_V1.6}$ or $\mathrm{Na_V1.2}$ in the AIS. In other words, results of sweeping x from 0 to 1 with κ fixed at 0.5 in Figure 4, Figure 5, Figure 2 are purely due to mixing and separating $\mathrm{Na_V1.6}$ from $\mathrm{Na_V1.2}$ in the AIS.

Since by definition $0 \leqslant \kappa \leqslant 1$ and $\sigma > 0$, the partial derivative of M with respect to κ is negative. It follows from Equation S10 that $\bar{G}_{\mathrm{Na_V1.2}}$ increases as the crossover position is moved distally. Likewise

$\bar{G}_{\mathrm{Na_V1.6}}$ decreases with increasing κ.

S1.6 Biophysics

Action potentials propagate via the cable equation

$$C\frac{\partial V}{\partial t} = \frac{d}{4R_a}\frac{d^2V}{ds^2} - I_{membrane}, \tag{S11}$$

where V is the membrane potential, C is the specific membrane capacitance, d is the neurite diameter, R_a is the axial resistance, s is position along the axis of the cable, and $I_{membrane}$ is the total transmembrane current density of all ion species in the model. Each compartment has explicit intracellular and extracellular concentrations of sodium, potassium, and chloride ions. We denote the intra/extra cellular concentration of a given ionic species "Z" as $[\mathrm{Z}]_{\mathrm{in}}$, $[\mathrm{Z}]_{\mathrm{out}}$ respectively. The Nernst potentials (reversal potentials) $E_{\mathrm{Na^+}}$, $E_{\mathrm{K^+}}$, $E_{\mathrm{Cl^-}}$ of $\mathrm{Na^+}$, $\mathrm{K^+}$, and $\mathrm{Cl^-}$ are not fixed parameters, but are instead determined by the intracellular and extracellular concentrations of those ions:

$$E_{\mathrm{Z}}(s) = -\frac{k_{\mathrm{B}}T}{q_{\mathrm{Z}}}\ln\left(\frac{[\mathrm{Z}]_{\mathrm{in}}}{[\mathrm{Z}]_{\mathrm{out}}}\right). \tag{S12}$$

Transmembrane concentration gradients of $\mathrm{Na^+}$ and $\mathrm{K^+}$ are governed by active transport ($\mathrm{Na^+}/\mathrm{K^+}$-pump) and longitudinal diffusion. At each time step, ionic concentrations all over the cell are updated using transmembrane currents (Equation S15) and Fick's law. At the jth compartment this gives:

$$\begin{cases} \dfrac{\partial}{\partial t}[\mathrm{Z}]^j_{\mathrm{in}} = -\left(\dfrac{A^j}{FVol^j_{\mathrm{in}}}\right)I^j_{\mathrm{Z}} + D_{\mathrm{Z}}\nabla^2[\mathrm{Z}]^j_{\mathrm{in}} \\[2ex] \dfrac{\partial}{\partial t}[\mathrm{Z}]^j_{\mathrm{out}} = \left(\dfrac{A^j}{FVol^j_{\mathrm{out}}}\right)I^j_{\mathrm{Z}} + D_{\mathrm{Z}}\nabla^2[\mathrm{Z}]^j_{\mathrm{out}}, \end{cases} \tag{S13}$$

where I^j_{Z} is the transmembrane current density of ion species Z at compartment j, with $\mathrm{Z} = \mathrm{Cl^-}, \mathrm{K^+}, \mathrm{Na^+}$. D_{Z} denotes the diffusion coefficient of ion Z. A^j and $Vol^j_{\mathrm{in(out)}}$ are (respectively) the membrane area and intracellular/extracellular volume at the jth compartment. The total transmembrane current density at

the jth compartment is

$$I^{j}_{membrane} = I^{j}_{\mathrm{Cl^-}} + I^{j}_{\mathrm{K^+}} + I^{j}_{\mathrm{Na^+}}. \tag{S14}$$

Omitting the compartment index j, the specific transmembrane currents are

$$I_{membrane} : \begin{cases} I_{\mathrm{Cl^-}} = g_{\mathrm{Cl^-}}(V - E_{\mathrm{Cl^-}}) \\ I_{\mathrm{K^+}} = (g_{\mathrm{K_V}} + g_{\mathrm{K,\ leak}})(V - E_{\mathrm{K^+}}) - 2I_{pump} \\ I_{\mathrm{Na^+}} = (g_{\mathrm{Na_V}} + g_{\mathrm{Na,\ leak}})(V - E_{\mathrm{Na^+}}) + 3I_{pump}. \end{cases} \tag{S15}$$

$g_{\mathrm{Cl^-}}$, $g_{\mathrm{K,\ leak}}$, and $g_{\mathrm{Na,\ leak}}$ are passive leak conductances whereas $g_{\mathrm{K_V}}$ and $g_{\mathrm{Na_V}}$ have voltage-gated Hodgkin-Huxley (HH)-style kinetics (Equation S17). Since channels are nonuniformly distributed along the cell membrane, conductances vary with location. I_{pump} is the net current produced by the $\mathrm{Na^+}/\mathrm{K^+}$-pump as a function of $[\mathrm{K^+}]_{\mathrm{out}}$ and $[\mathrm{Na^+}]_{\mathrm{in}}$,

$$I_{pump} = I_{maxpump}\left(1 + \frac{K_{M_{\mathrm{K^+}}}}{[\mathrm{K^+}]_{\mathrm{out}}}\right)^{-2}\left(1 + \frac{K_{M_{\mathrm{Na^+}}}}{[\mathrm{Na^+}]_{\mathrm{in}}}\right)^{-3}, \tag{S16}$$

where $I_{maxpump}$ is the maximal current generated by the pump, $K_{M_{\mathrm{K^+}}}$ and $K_{M_{\mathrm{Na^+}}}$ are Michaelis-Menten kinetic constants, and the $\mathrm{Na^+}$ and $\mathrm{K^+}$ currents flowing through the pump are $I_{\mathrm{Na^+},pump} = 3I_{pump}$ and $I_{\mathrm{K^+},pump} = -2I_{pump}$.

S1.7 Voltage-Gated Channels

The voltage-gated sodium and potassium conductances $g_{\mathrm{Na_V}}(V,t)$ and $g_{\mathrm{K_V}}(V,t)$ in Equation S15 are modelled using HH-style kinetics Hodgkin and Huxley (1952) fitted to mammalian pyramidal cell data by Mainen et al. (1995), and then further adapted by Hu et al. (2009) to include two $\mathrm{Na_V}$ variants (Equation S18). In the Hodgkin-Huxley model the current density I_{Z} of ion species "Z" through voltage-gated channels of a given type is

$$I_{\mathrm{Z_V}} = \bar{g}_{\mathrm{Z_V}} m^p h^q (V - E_{\mathrm{Z}}), \tag{S17}$$

where $\bar{g}$ is the maximal conductance, $m(V,t)$ is the probability for an activation gate to be open, p is the number of activation gates per channel, $h(V,t)$ is the *availability* (probability that the channel is *not*

inactivated), and q is the number of inactivation gates per channel. $\mathrm{Na_V}$ channels are modelled as having three activation gates ($p = 3$) and a single inactivation gate ($q = 1$) so that $g_{\mathrm{Na_V}} \propto m^3 h$. Likewise, $\mathrm{K_V}$ channels have a single activation gate and no inactivation ($g_{\mathrm{K_V}} \propto n$). The gating variables m, h, and n evolve according to Equations S1, S2, and S3. Since the cell features two $\mathrm{Na_V}$ subtypes ($\mathrm{Na_V}1.2$ and $\mathrm{Na_V}1.6$), the model computes two sets of sodium activation and *availability* variables. The current density I_{Na} through the $\mathrm{Na_V}$ channels is then

$$I_{\mathrm{Na_V}} = \left(\underbrace{\bar{g}_{\mathrm{Na_V}1.2} (m^{\mathrm{Na_V}1.2})^3 h^{\mathrm{Na_V}1.2}}_{g_{\mathrm{Na_V}1.2}} + \underbrace{\bar{g}_{\mathrm{Na_V}1.6} (m^{\mathrm{Na_V}1.6})^3 h^{\mathrm{Na_V}1.6}}_{g_{\mathrm{Na_V}1.6}} \right) (V - E_{\mathrm{Na}^+}), \tag{S18}$$

where $g_{\mathrm{Na_V}1.2} + g_{\mathrm{Na_V}1.6} = g_{\mathrm{Na_V}}$ in Equation S15.

Figure S7 plots the voltage-dependent kinetics of $m^{\mathrm{Na_V}1.2}$, $h^{\mathrm{Na_V}1.2}$, $m^{\mathrm{Na_V}1.6}$ and $h^{\mathrm{Na_V}1.6}$. The steady-state activation and *availability* functions and their voltage-sensitive time constants were implemented using the parameters provided in Hu et al. (2009) and in model code published by Mainen and Sejnowski (1996). We further modified the channel models to allow shift-clamping, see Section 3.2.4 and Section S1.1.

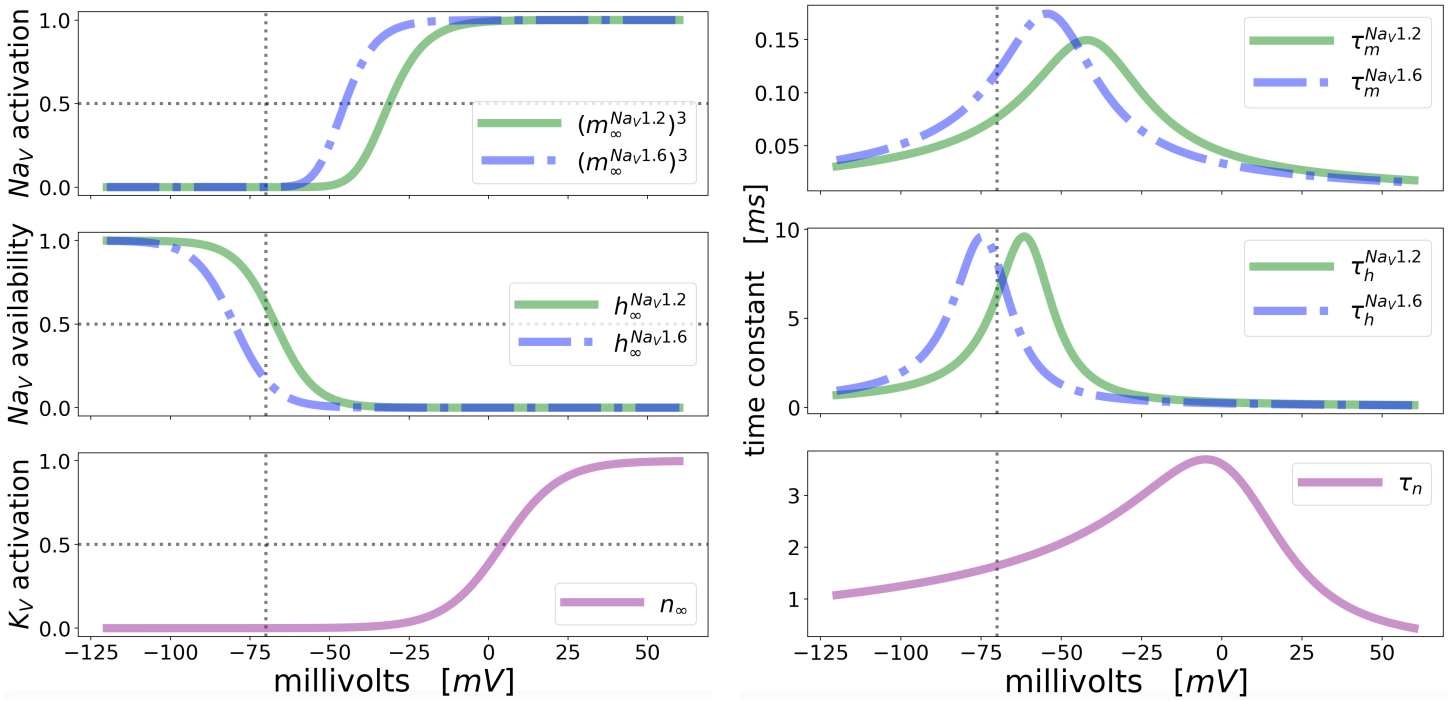

(a) (b)

Figure S7: Gating properties of the voltage-gated sodium and potassium channels implemented in this model. Dotted vertical lines indicate the resting potential V_{rest}. (a) Steady-state *activation* and *availability* curves for $\text{Na}_\text{V}1.2$ and $\text{Na}_\text{V}1.6$, and steady-state K_V *activation*. (b) Voltage-sensitive time constants of $\text{Na}_\text{V}1.2$, $\text{Na}_\text{V}1.6$, and K_V. $\text{Na}_\text{V}1.2$ is intrinsically *right-shift*ed by an amount V_{RS} relative to $\text{Na}_\text{V}1.6$ (defined in Section S1.7.1). In this model $V_{\text{RS}} = 13.0\text{mV}$.

The intrinsic *right-shift* of $\text{Na}_\text{V}1.2$ (defined mathematically in Section S1.7.1) is easiest to observe in the top two plots of Figure S7a. Steady-state activation $\left(m_\infty^{\text{Na}_\text{V}1.2}(V)\right)^3$ and *availability* $h_\infty^{\text{Na}_\text{V}1.2}(V)$ curves of $\text{Na}_\text{V}1.2$ are plotted as solid green lines, and dashed blue lines are the corresponding curves for $\text{Na}_\text{V}1.6$. The voltage shift separating Na_V activation curves is approximately V_{RS}, though it varies with position since the gating variables of Na_V activation ($m^{\text{Na}_\text{V}1.2}$, $m^{\text{Na}_\text{V}1.6}$) are raised to the third power and do not have identical slope Hu et al. (2009). However, the *availability* curves are much easier to compare: in this model $h_\infty^{\text{Na}_\text{V}1.2}(V)$ is shifted exactly $V_{\text{RS}} = 13.0\text{mV}$ to the right of $h_\infty^{\text{Na}_\text{V}1.6}(V)$. The intrinsic *right-shift* of $\text{Na}_\text{V}1.2$ is also visible in the voltage-sensitive time constants (Figure S7b).

S1.7.1 Defining V_{RS}: the intrinsic *right-shift* of $\text{Na}_\text{V}1.2$

V_{RS} is a parameter in this model which represents the experimentally measured depolarizing shift in the voltage dependence of $\text{Na}_\text{V}1.2$ activation and inactivation kinetics, relative to $\text{Na}_\text{V}1.6$ kinetics. Because

V_{RS} is empirical, it is fixed in this paper.

We define the $\mathrm{Na_V1.6}$ half-*activation* voltage $V_{1/2}^{\mathrm{Na_V1.6}}$ as the voltage at which a single $\mathrm{Na_V1.6}$ activation gate (randomly selected from an ensemble of gates held at $V = V_{1/2}^{\mathrm{Na_V1.6}}$) has a 50% chance of being in the open state:

$$m_{\infty}^{\mathrm{Na_V1.6}}(V_{1/2}^{\mathrm{Na_V1.6}}) \stackrel{\text{def}}{=} \frac{1}{2}.$$

Although the kinetics of $\mathrm{Na_V1.2}$ differ from $\mathrm{Na_V1.6}$ kinetics in ways *other than right-shift*, we can now use $V_{1/2}^{\mathrm{Na_V1.6}}$ to define V_{RS} as the voltage that satisfies

$$\boxed{m_{\infty}^{\mathrm{Na_V1.2}}(V_{1/2}^{\mathrm{Na_V1.6}} + V_{\mathrm{RS}}) = m_{\infty}^{\mathrm{Na_V1.6}}(V_{1/2}^{\mathrm{Na_V1.6}}) = \frac{1}{2}}. \tag{S19}$$

Note that $V_{1/2}^{\mathrm{Na_V1.6}}$ and V_{RS} are unique since m_{∞} is monotonically increasing. Equation S19 also contains the half-*activation* voltage for $\mathrm{Na_V1.2}$,

$$V_{1/2}^{\mathrm{Na_V1.2}} = V_{1/2}^{\mathrm{Na_V1.6}} + V_{\mathrm{RS}}, \tag{S20}$$

which is depolarized or "right-shifted" by an amount V_{RS} relative to $\mathrm{Na_V1.6}$ (see Figure S7).

To simulate alterations to $\mathrm{Na_V1.2}$ *right-shift* in our shift-clamping method, we use another parameter called ΔV_{RS}, which is not based on experiment. Although the intrinsic $\mathrm{Na_V1.2}$ *right-shift* is not a high precision measurement ($V_{\mathrm{RS}} \sim 10 - 15\mathrm{mV}$), the *parameter* V_{RS} is kept fixed in our model for conceptual purposes: we find it useful to distinguish empirical parameters (like V_{RS}) from exploratory parameters that intentionally deviate from experiment (like ΔV_{RS}). In fact we use ΔV_{RS} to selectively change the model's $\mathrm{Na_V}$ kinetics (see Section S1.1), to explain the effects of $\mathrm{Na_V}$ distribution on excitability in terms of gating properties (Section 3.2.4).

S1.7.2 Notation: V_{RS}, ΔV_{RS}

In our notation, V_{RS} is *not written explicitly* in the argument of $\mathrm{Na_V1.2}$ gating variables or their time constants. Instead we write

$$\tau_h^{\mathrm{Na_V1.2}}(V),\ \tau_h^{\mathrm{Na_V1.6}}(V), \text{ et cetera,}$$

and let the superscript "$^{\mathrm{Na_V1.2}}$" indicate that $\tau_h^{\mathrm{Na_V1.2}}$ is *right-shift*ed relative to $\tau_h^{\mathrm{Na_V1.6}}$, from the fact that $\mathrm{Na_V1.2}$ channels are *right-shift*ed.

However, the parameter ΔV_{RS} *is* written explicitly in the argument when we model the effects of modifying the *right-shift* (Figure 6: shift-clamping). For example, when applying $\Delta V_{\mathrm{RS}} \neq 0$ to the *selected* kinetic variables $\tau_h^{\mathrm{Na_V1.2}}$ and $m_\infty^{\mathrm{Na_V1.2}}$, we would write

$$\begin{cases} \tau_h^{\mathrm{Na_V1.2}} = \tau_h^{\mathrm{Na_V1.2}}(V - \Delta V_{\mathrm{RS}}) \\ h_\infty^{\mathrm{Na_V1.2}} = h_\infty^{\mathrm{Na_V1.2}}(V) \\ \tau_m^{\mathrm{Na_V1.2}} = \tau_m^{\mathrm{Na_V1.2}}(V) \\ m_\infty^{\mathrm{Na_V1.2}} = m_\infty^{\mathrm{Na_V1.2}}(V - \Delta V_{\mathrm{RS}}). \end{cases} \tag{S21}$$

Using this notation, positive values of ΔV_{RS} will shift kinetic curves to the right (depolarizing shift) and negative ΔV_{RS} produces a hyperpolarizing shift.

S1.7.3 Space plots of $\mathrm{Na_V}$ kinetics along the AIS — steady-state

The distribution of $\mathrm{Na_V1.2}$ and $\mathrm{Na_V1.6}$ in the AIS creates a lengthwise distribution of gating properties. Proximal $\mathrm{Na_V1.2}$ increases local steady-state *availability*, owing to these channels' intrinsic *right-shift* (V_{RS}). In Figure S8a we visualize this effect using $\mathcal{H}(s)$: the net *availability* of $\mathrm{Na_V}$s ($\mathcal{H}$) as a function of position (s), computed by weighting $h^{\mathrm{Na_V1.2}}$ and $h^{\mathrm{Na_V1.6}}$ according to their respective local $\mathrm{Na_V}$ channel densities:

$$\mathcal{H}(s,t) = \frac{\bar{g}_{\mathrm{Na_V1.2}}(s) h^{\mathrm{Na_V1.2}}(s,t) + \bar{g}_{\mathrm{Na_V1.6}}(s) h^{\mathrm{Na_V1.6}}(s,t)}{\bar{g}_{\mathrm{Na_V1.2}}(s) + \bar{g}_{\mathrm{Na_V1.6}}(s)}. \tag{S22}$$

An effective local $\mathrm{Na_V}$ time constant of *availability* ($\boldsymbol{\mathcal{T}}$) can be computed from $\tau_h^{\mathrm{Na_V1.2}}$ and $\tau_h^{\mathrm{Na_V1.6}}$ as

$$\boldsymbol{\mathcal{T}}(s,t) = \frac{\bar{g}_{\mathrm{Na_V1.2}}(s) \tau_h^{\mathrm{Na_V1.2}}(s,t) + \bar{g}_{\mathrm{Na_V1.6}}(s) \tau_h^{\mathrm{Na_V1.6}}(s,t)}{\bar{g}_{\mathrm{Na_V1.2}}(s) + \bar{g}_{\mathrm{Na_V1.6}}(s)}. \tag{S23}$$

Above we have abbreviated

$$f(V(s,t),t) = f(s,t) \text{ for } f = h^{\mathrm{Na_V1.2}}, h^{\mathrm{Na_V1.6}}, \tau_h^{\mathrm{Na_V1.2}}, \tau_h^{\mathrm{Na_V1.6}}. \tag{S24}$$

In Figure S8b we have selectively disabled the *right-shift* of $\tau_h^{\mathrm{Na_V1.2}}$ by setting $\Delta V_{\mathrm{RS}} = -V_{\mathrm{RS}} = -13.0\mathrm{mV}$ in Equation 1, which leaves the *right-shift* of steady-state *availability* unchanged.

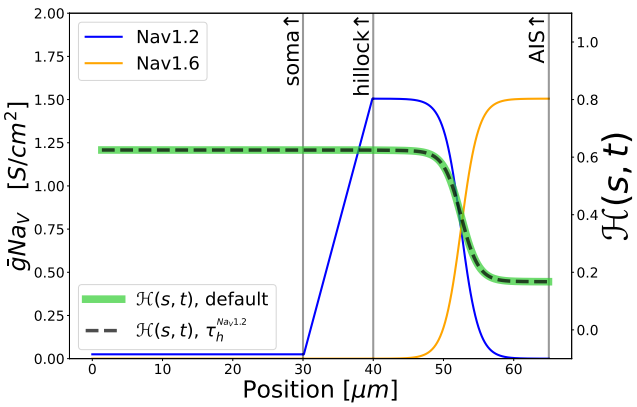

(a) Solid green curve: Travelling from the soma to the hillock and across the AIS, $\mathrm{Na_V1.6}$ overtakes $\mathrm{Na_V1.2}$ as a share of the total local $\mathrm{Na_V}$ density. The accompanying change in $\mathrm{Na_V}$ *right-shift* causes $\mathcal{H}(s)$ to drop from ≈ 0.6 at the soma and proximal AIS, down to ≈ 0.2 at the distal AIS and axon. Dashed black curve: the *right-shift* of $\tau_h^{\mathrm{Na_V1.2}}$ has been selectively disabled without altering $h_\infty^{\mathrm{Na_V1.2}}$, and thereby $\mathcal{H}$ is also unaffected. See Figure S8b to the right as well as Equation 1.

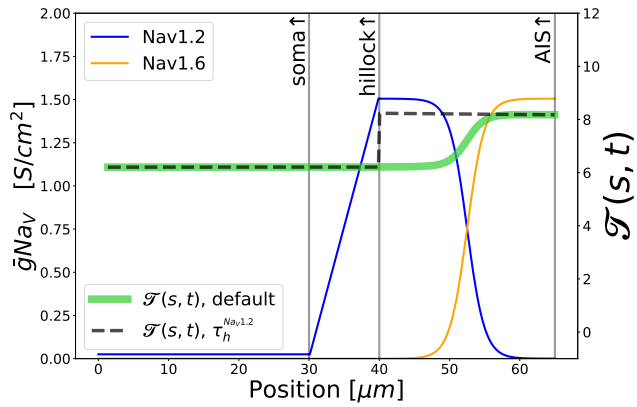

(b) Solid green curve: Where $\mathrm{Na_V1.6}$ overtakes $\mathrm{Na_V1.2}$ as a share of the total local $\mathrm{Na_V}$ density, $\boldsymbol{\mathcal{T}}(s)$ increases from $\approx 6\mathrm{ms}$ to $\approx 8\mathrm{ms}$. Dashed black curve: *right-shift* of $\tau_h^{\mathrm{Na_V1.2}}$ selectively disabled by setting $\Delta V_{\mathrm{RS}} = -V_{\mathrm{RS}}$ in Equation 1. The effective time constant of $\mathrm{Na_V}$ *availability* $\boldsymbol{\mathcal{T}}(s)$ is now uniform along the AIS. The abrupt transition in $\boldsymbol{\mathcal{T}}$ at the AIS-hillock interface —instead of the smooth transition along the AIS in the green curve— is due to V_{RS} of $\tau_h^{\mathrm{Na_V1.2}}(V)$ being selectively disabled —see Equation S23. The *right-shift* of $h_\infty^{\mathrm{Na_V1.2}}(V)$ has not been altered (see Equation S22), and the corresponding $\mathcal{H}$ (dashed black) curve in Figure S8a is unchanged —hence the term "selective".

Figure S8: The effect of $\mathrm{Na_V1.2}$ *right-shift* on local $\mathrm{Na_V}$ *availability* along the cell is visible in space plots of steady-state total *availability* $\mathcal{H}(s)$ (S8a) and total time constant $\boldsymbol{\mathcal{T}}(s)$ (S8b) at $V = V_{\mathrm{rest}}$. See Equation S22 and Equation S23 respectively.

S1.8 Diffusion Coefficients

Diffusion coefficients for Na^+, K^+, and Cl^- in water at 25.0 ℃ are provided by Samson et al. (2003) :

$$\begin{cases} D_{\mathrm{Na}^+} = 1.334 \times 10^{-9} \dfrac{\mathbf{m}^2}{\mathbf{s}} \\ D_{\mathrm{K}^+} = 1.957 \times 10^{-9} \dfrac{\mathbf{m}^2}{\mathbf{s}} \\ D_{\mathrm{Cl}^-} = 2.032 \times 10^{-9} \dfrac{\mathbf{m}^2}{\mathbf{s}}. \end{cases} \tag{S25}$$

Our simulations are done at a warmer temperature, so these coefficients need to be adjusted. We make the adjustment using the Stokes-Einstein equation

$$D = \frac{k_B T}{\zeta(T)} = \frac{k_B T}{6\pi r \eta(T)} \; ; \tag{S26}$$

where k_B is Boltzmann's constant, T is temperature (Kelvins $\mathbf{K}$), and ζ is called the drag coefficient. ζ is given by the ion's radius r and the viscosity $\eta(T)$ of the medium (liquid water) which depends on temperature. Hence the ratio of diffusion coefficients for ion species Z at T_2 and T_1 is

$$\frac{D_{\mathrm{Z}}(T_2)}{D_{\mathrm{Z}}(T_1)} = \left(\frac{T_2}{T_1}\right)\left(\frac{\eta(T_1)}{\eta(T_2)}\right), \tag{S27}$$

with T_2 and T_1 converted to $\mathbf{K}$. The reference values provided by Samson et al. (2003) are measured at $298.15\mathbf{K}$ (25.0℃), and the simulation temperature is $310.15\mathbf{K}$ (37.0℃). Assuming the viscosity of water, we have $\eta(T_1) \cong 0.89$ $\mathtt{m}\mathbf{Pa\ s}$ and $\eta(T_2) \cong 0.691$ $\mathtt{m}\mathbf{Pa\ s}$. Substituting these η's into Equation S27 gives for each ionic species Z

$$\underbrace{D_{\mathrm{Z}}(310.15\mathbf{K})}_{37.0℃} \cong 1.34 \times \underbrace{D_{\mathrm{Z}}(298.15\mathbf{K})}_{25.0℃}, \tag{S28}$$

which yields the temperature adjusted diffusion coefficients

$$\begin{cases} D_{\mathrm{Na}^+} = 1.79 \times 10^{-9} \dfrac{\mathbf{m}^2}{\mathbf{s}} \\ D_{\mathrm{K}^+} = 2.62 \times 10^{-9} \dfrac{\mathbf{m}^2}{\mathbf{s}} \\ D_{\mathrm{Cl}^-} = 2.72 \times 10^{-9} \dfrac{\mathbf{m}^2}{\mathbf{s}}. \end{cases} \tag{S29}$$

S1.9 Tables of parameters

In the following tables, we compare our model to previous models on which it is based (Mainen et al. (1995), Mainen and Sejnowski (1996), Hu et al. (2009)). At different locations in the cell, we list key parameter values from these papers alongside our own. We also include certain measurements (membrane potential, ion concentrations, Nernst potentials) taken from our model at each location once the cell has equilibrated.

The following symbols are used in the tables: (Units are given in the tables.)

"×" This symbol appears when a parameter is not featured in the model corresponding to a given column.

$V_{\mathbf{rest}}$ Resting potential. The transmembrane voltage of the model neuron at steady-state with no injected current.

$V_{\mathbf{m}}^{\mathbf{location}}$ Transmembrane voltage at 'location'. In our model, the steady-state transmembrane voltage is actively maintained everywhere by Na^+/K^+-pumps and longitudinal diffusion which control the explicit intracellular and extracellular ion concentrations. As such, the tabulated values are *recorded* from the model, not parameters per-say. In the other models listed, V_{m} is identical to V_{rest}.

$R_{\mathbf{axial}}$ Axial resistance. The resistance to axial current flow across a compartment is R_{axial} multiplied by the compartment length, divided by the compartment's cross-sectional area.

$D_{\mathbf{ion}}$ Diffusion coefficient of the specified ion in water at $37°\mathrm{C}$.

$T_{\mathbf{ref}}$ Reference temperature of experimentally developed channel properties used in the models. Past modeling, on which this paper is based, used temperature factors (described below) to adjust channel densities and speed up channel kinetics to warmer temperatures.

T Simulation temperature.

$Q_{\bar{g}_{\mathbf{V}}}^{\mathbf{Mainen}} = Q_{10,\bar{g}_{\mathbf{V}}}^{(T-T_{\mathbf{ref}})/10°\mathrm{C}}$ To adjust for a warmer simulation temperature of $T = 37°\mathrm{C}$ Mainen and Sejnowski (1996) scale up their maximal voltage-gated conductances, which were originally developed at $T = 23°\mathrm{C}$ (Mainen et al. (1995)), by a factor which we denote $Q_{\mathrm{Mainen}}^{\bar{g}_{\mathrm{V}}}$. They warn in their model code that this scaling is valid only at $37°\mathrm{C}$, and state that their program is not designed to model other temperatures. This internal temperature scaling can accidentally obscure parameter settings

when one attempts to borrow parameters separately from the past code, or from later papers that reuse these channel models. For this reason we have removed the temperature scaling from our own model code by setting our reference temperature equal to the simulation temperature, which sets $Q_{\text{Mainen}}^{\bar{g}_{\text{V}}} = 1$.

$\bar{g}_{\mathbf{Na_V \cdot Total}}^{\mathbf{location}}$ Total combined maximal voltage-gated conductance density of $\text{Na}_\text{V}1.2$ and $\text{Na}_\text{V}1.6$ at the specified 'location' in the cell (see Equation S7). The location can be an entire Section if the membrane properties are uniform (in NEURON, Sections consist of multiple compartments). For example, somatodendritic channel densities are uniform in this model, so 'soma' is sufficient to specify those parameters.

$\bar{g}_{\mathbf{K_V \cdot Total}}^{\mathbf{location}}$ Maximal voltage-gated K^+ conductance density at the specified 'location'.

$C_{\mathbf{m}}$ Membrane capacitance per unit area. Applies everywhere except at internodes.

$C_{\mathbf{m}}^{\mathbf{myelin}}$ Membrane capacitance of myelinated internodes.

$L_{\mathbf{Section}}$ Length of the specified 'Section' (soma, hillock, AIS, etc.)

$d_{\mathbf{Section}}^{\mathbf{position\ within\ Section}}$ Diameter at a given normalized position $(0 \leqslant s \leqslant 1)$ within the specified Section (soma, hillock, AIS, etc.). The position is not specified when the diameter is uniform.

$R_{\mathbf{Passive}}^{\mathbf{Section}}$ Membrane resistivity in 'Section'.

$g_{\mathbf{Passive}}^{\mathbf{Section}}$ Passive generic transmembrane leak conductance density in 'Section'.

$g_{\mathbf{Ion,\ leak}}^{\mathbf{Section}}$ Specific leak conductance density of 'Ion' in 'Section'.

$I_{\mathbf{MaxPump}}^{\mathbf{Section}}$ Maximum Na^+/K^+-pump current density in 'Section'.

$E_{\mathbf{current\ type}}^{\mathbf{Section}}$ Nernst Potential (reversal potential) of transmembrane current 'current type' (e.g. 'leak') in 'Section' (e.g. 'soma').

$[\mathbf{Ion}]_{\mathbf{in/out}}^{\mathbf{Section}}$ Intracellular ('in') or Extracellular ('out') concentration of 'Ion' at 'Section', with the neuron at steady-state. Because these concentrations are maintained by Na^+/K^+-pumps and longitudinal diffusion in our model, the concentrations tabulated here are measurements *recorded* from the simulation at steady-state, rather than being fixed parameters.

ranvier0, myelin0: In our model, there are 15 nodes of Ranvier and 16 myelinated internodes. The Section named 'ranvier0' is the first node of Ranvier. And 'myelin0' is the first myelinated internode of the axon, located between the distal end of the AIS (or the distal end of the bare axon when that is included) and the proximal end of ranvier0.

Type	Parameter Name	OurModel	Mainen95	Mainen96	Hu2009	units
Global						
	V_{rest}	-70.0	-70.0	-70.0	-70.0	mV
	R_{axial}	150	200	150	150	$\Omega \cdot \mathrm{cm}$
	D_{Cl^-}	2.72	×	×	×	$10^{-9}\frac{\mathrm{m}^2}{\mathrm{s}}$
	D_{Na^+}	1.79	×	×	×	$10^{-9}\frac{\mathrm{m}^2}{\mathrm{s}}$
	D_{K^+}	2.62	×	×	×	$10^{-9}\frac{\mathrm{m}^2}{\mathrm{s}}$
	T_{ref}	37.0	23.0	23.0	23.0	℃
	T	37.0	23.0	37.0	37.0	℃
	$Q_{\bar{g}_{\text{V}}}^{\text{Mainen}} = Q_{10,\bar{g}_{\text{V}}}^{(T-T_{\text{ref}})/10℃}$	1.0	1.0	3.21	3.21	dimensionless
	C_{m}	0.75	0.75	0.75	1.0	$\frac{\mu F}{\mathrm{cm}^2}$
	$C_{\text{m}}^{\text{myelin}}$	0.02	0.04	0.02	0.02	$\frac{\mu F}{\mathrm{cm}^2}$

Geometry

L_{soma}	30.0	25.8	30.0	30.0	μm
L_{hillock}	10.0	10.0	10.0	10.0	μm
L_{AIS}	100.0	15.0	15.0	50.0	μm
$L_{\text{bare·axon}}$	400	×	×	400	μm
$d^{0.5}_{\text{soma}}$	19.38	15.2	19.0	19.0	μm
$d^{1.0}_{\text{soma}}$	8.62	15.2	8.6	8.6	μm
$d^{0.0}_{\text{hillock}}$	8.62	4.0	4.0	3.8	μm
$d^{1.0}_{\text{hillock}}$	1.22	1.0	1.0	2.4	μm
d_{AIS}	1.22	1.0	1.0	1.22	μm
$d_{\text{bare·axon}}$	1.22	×	×	1.02	μm

section	Parameter Name	OurModel	Mainen95	Mainen96	Hu2009	units
soma						
	$\bar{g}^{\text{soma}}_{\text{Na}_\text{V}\cdot\text{Total}}$	2.51×10^{-2}	0.003	0.002	0.008	$\frac{\mho}{\text{cm}^2}$
	$\bar{g}^{\text{soma}}_{\text{Na}_\text{V}\cdot\text{Total}} \times Q^{\text{Mainen}}_{\bar{g}_\text{V}}$	2.51×10^{-2}	3.00×10^{-3}	6.42×10^{-3}	2.57×10^{-2}	$\frac{\mho}{\text{cm}^2}$

$\bar{g}_{\mathrm{K_V}}^{\mathrm{soma}}$	7.53×10^{-3}	0.01	0.02	0.002	$\frac{\mho}{\mathrm{cm}^2}$
$\bar{g}_{\mathrm{K_V}}^{\mathrm{soma}} \times Q_{\bar{g}_{\mathrm{V}}}^{\mathrm{Mainen}}$	7.53×10^{-3}	1.00×10^{-2}	6.42×10^{-2}	6.42×10^{-3}	$\frac{\mho}{\mathrm{cm}^2}$
$R_{\mathrm{Passive}}^{\mathrm{soma}}$	7.16×10^{3}	4.00×10^{4}	3.00×10^{4}	3.00×10^{4}	$\Omega \cdot \mathrm{cm}^2$
$g_{\mathrm{Passive}}^{\mathrm{soma}}$	1.40×10^{-4}	2.50×10^{-5}	3.33×10^{-5}	3.33×10^{-5}	$\frac{\mho}{\mathrm{cm}^2}$
$g_{\mathrm{Cl^-,\ leak}}^{\mathrm{soma}}$	2.09×10^{-5}	×	×	×	$\frac{\mho}{\mathrm{cm}^2}$
$g_{\mathrm{Na^+,\ leak}}^{\mathrm{soma}}$	2.23×10^{-5}	×	×	×	$\frac{\mho}{\mathrm{cm}^2}$
$g_{\mathrm{K^+,\ leak}}^{\mathrm{soma}}$	9.66×10^{-5}	×	×	×	$\frac{\mho}{\mathrm{cm}^2}$
$I_{\mathrm{MaxPump}}^{\mathrm{soma}}$	1.33×10^{-2}	×	×	×	$\frac{\mathrm{mA}}{\mathrm{cm}^2}$
$V_{\mathrm{m}}^{\mathrm{soma}}$	-70.2	-70.0	-70.0	-70.0	mV
$E_{\mathrm{leak}}^{\mathrm{soma}}$	×	-70.0	-70.0	-70.0	mV
$E_{\mathrm{Cl}}^{\mathrm{soma}}$	-70.0	×	×	×	mV
$E_{\mathrm{Na}}^{\mathrm{soma}}$	60.0	60.0	50.0	60.0	mV
$E_{\mathrm{K}}^{\mathrm{soma}}$	-90.0	-90.0	-90.0	-90.0	mV
$[\mathrm{Cl^-}]_{\mathrm{in}}^{\mathrm{soma}}$	11.0	×	×	×	mM
$[\mathrm{Cl^-}]_{\mathrm{out}}^{\mathrm{soma}}$	151.0	×	×	×	mM

	$[\mathrm{Na}^+]_{\mathrm{in}}^{\mathrm{soma}}$	15.0	×	×	×	mM
	$[\mathrm{Na}^+]_{\mathrm{out}}^{\mathrm{soma}}$	141.6	×	×	×	mM
	$[\mathrm{K}^+]_{\mathrm{in}}^{\mathrm{soma}}$	140.0	×	×	×	mM
	$[\mathrm{K}^+]_{\mathrm{out}}^{\mathrm{soma}}$	4.8	×	×	×	mM
section	Parameter Name	OurModel	Mainen95	Mainen96	Hu2009	units
AIS						
	$\bar{g}_{\mathrm{Na_V}\cdot\mathrm{Total}}^{\mathrm{AIS}}$	1.505	3.0	3.0	0.32	$\frac{\mho}{\mathrm{cm}^2}$
	$\bar{g}_{\mathrm{Na_V}\cdot\mathrm{Total}}^{\mathrm{AIS}} \times Q_{\bar{g}_{\mathrm{V}}}^{\mathrm{Mainen}}$	1.505	3.0	9.628	1.027	$\frac{\mho}{\mathrm{cm}^2}$
	$\bar{g}_{\mathrm{K_V}}^{\mathrm{AIS}}$	4.52×10^{-1}	×	0.2	0.1	$\frac{\mho}{\mathrm{cm}^2}$
	$\bar{g}_{\mathrm{K_V}}^{\mathrm{AIS}} \times Q_{\bar{g}_{\mathrm{V}}}^{\mathrm{Mainen}}$	4.52×10^{-1}	×	6.42×10^{-1}	3.21×10^{-1}	$\frac{\mho}{\mathrm{cm}^2}$
	$R_{\mathrm{Passive}}^{\mathrm{AIS}}$	4.77×10^{1}	5.00×10^{1}	5.00×10^{1}	5.00×10^{1}	$\Omega \cdot \mathrm{cm}^2$
	$g_{\mathrm{Passive}}^{\mathrm{AIS}}$	2.10×10^{-2}	2.00×10^{-2}	2.00×10^{-2}	2.00×10^{-2}	$\frac{\mho}{\mathrm{cm}^2}$
	$g_{\mathrm{Cl^-,\ leak}}^{\mathrm{AIS}}$	3.14×10^{-3}	×	×	×	$\frac{\mho}{\mathrm{cm}^2}$
	$g_{\mathrm{Na^+,\ leak}}^{\mathrm{AIS}}$	3.34×10^{-3}	×	×	×	$\frac{\mho}{\mathrm{cm}^2}$

	$g^{\mathrm{AIS}}_{\mathrm{K^+,\ leak}}$	1.45×10^{-2}	×	×	×	$\frac{\mho}{\mathrm{cm}^2}$
	$I^{\mathrm{AIS}}_{\mathrm{MaxPump}}$	1.995	×	×	×	$\frac{\mathrm{mA}}{\mathrm{cm}^2}$
	$V^{\mathrm{AIS}}_{\mathrm{m}}$	−69.9	−70.0	−70.0	−70.0	mV
	$E^{\mathrm{AIS}}_{\mathrm{leak}}$	×	−70.0	−70.0	−70.0	mV
	$E^{\mathrm{AIS}}_{\mathrm{Cl}}$	−70.0	×	×	×	mV
	$E^{\mathrm{AIS}}_{\mathrm{Na}}$	59.9	60.0	50.0	60.0	mV
	$E^{\mathrm{AIS}}_{\mathrm{K}}$	−90.0	−90.0	−90.0	−90.0	mV
	$[\mathrm{Cl^-}]^{\mathrm{AIS}}_{\mathrm{in}}$	11.0	×	×	×	mM
	$[\mathrm{Cl^-}]^{\mathrm{AIS}}_{\mathrm{out}}$	151.0	×	×	×	mM
	$[\mathrm{Na^+}]^{\mathrm{AIS}}_{\mathrm{in}}$	15.1	×	×	×	mM
	$[\mathrm{Na^+}]^{\mathrm{AIS}}_{\mathrm{out}}$	141.6	×	×	×	mM
	$[\mathrm{K^+}]^{\mathrm{AIS}}_{\mathrm{in}}$	139.9	×	×	×	mM
	$[\mathrm{K^+}]^{\mathrm{AIS}}_{\mathrm{out}}$	4.8	×	×	×	mM

section	Parameter Name	OurModel	Mainen95	Mainen96	Hu2009	units
myelin0						

$\bar{g}^{\text{myelin0}}_{\text{Na}_\text{V}\cdot\text{Total}}$	1.61×10^{-2}	0.003	×	0.002	$\frac{\mho}{\text{cm}^2}$
$\bar{g}^{\text{myelin0}}_{\text{Na}_\text{V}\cdot\text{Total}} \times Q^{\text{Mainen}}_{\bar{g}_\text{V}}$	1.61×10^{-2}	3.00×10^{-3}	×	6.42×10^{-3}	$\frac{\mho}{\text{cm}^2}$
$\bar{g}^{\text{myelin0}}_{\text{K}_\text{V}}$	4.82×10^{-3}	×	×	×	$\frac{\mho}{\text{cm}^2}$
$\bar{g}^{\text{myelin0}}_{\text{K}_\text{V}} \times Q^{\text{Mainen}}_{\bar{g}_\text{V}}$	4.82×10^{-3}	×	×	×	$\frac{\mho}{\text{cm}^2}$
$R^{\text{myelin0}}_{\text{Passive}}$	1.12×10^{4}	4.00×10^{4}	3.00×10^{4}	3.00×10^{4}	$\Omega \cdot \text{cm}^2$
$g^{\text{myelin0}}_{\text{Passive}}$	8.94×10^{-5}	2.50×10^{-5}	3.33×10^{-5}	3.33×10^{-5}	$\frac{\mho}{\text{cm}^2}$
$g^{\text{myelin0}}_{\text{Cl}^-,\text{ leak}}$	1.34×10^{-5}	×	×	×	$\frac{\mho}{\text{cm}^2}$
$g^{\text{myelin0}}_{\text{Na}^+,\text{ leak}}$	1.43×10^{-5}	×	×	×	$\frac{\mho}{\text{cm}^2}$
$g^{\text{myelin0}}_{\text{K}^+,\text{ leak}}$	6.18×10^{-5}	×	×	×	$\frac{\mho}{\text{cm}^2}$
$I^{\text{myelin0}}_{\text{MaxPump}}$	8.51×10^{-3}	×	×	×	$\frac{\text{mA}}{\text{cm}^2}$
$V^{\text{myelin0}}_{\text{m}}$	-69.4	-70.0	-70.0	-70.0	mV
$E^{\text{myelin0}}_{\text{leak}}$	×	-70.0	-70.0	-70.0	mV
$E^{\text{myelin0}}_{\text{Cl}}$	-70.0	×	×	×	mV
$E^{\text{myelin0}}_{\text{Na}}$	60.0	60.0	50.0	60.0	mV
$E^{\text{myelin0}}_{\text{K}}$	-90.0	-90.0	-90.0	-90.0	mV

	$[\mathrm{Cl}^-]_{\mathrm{in}}^{\mathrm{myelin0}}$	11.0	×	×	×	mM
	$[\mathrm{Cl}^-]_{\mathrm{out}}^{\mathrm{myelin0}}$	151.0	×	×	×	mM
	$[\mathrm{Na}^+]_{\mathrm{in}}^{\mathrm{myelin0}}$	15.0	×	×	×	mM
	$[\mathrm{Na}^+]_{\mathrm{out}}^{\mathrm{myelin0}}$	141.6	×	×	×	mM
	$[\mathrm{K}^+]_{\mathrm{in}}^{\mathrm{myelin0}}$	140.0	×	×	×	mM
	$[\mathrm{K}^+]_{\mathrm{out}}^{\mathrm{myelin0}}$	4.8	×	×	×	mM
section	Parameter Name	OurModel	Mainen95	Mainen96	Hu2009	units
ranvier0						
	$\bar{g}_{\mathrm{Na_V}\cdot\mathrm{Total}}^{\mathrm{ranvier0}}$	8.03×10^{-1}	3.0	3.0	0.16	$\frac{\mho}{\mathrm{cm}^2}$
	$\bar{g}_{\mathrm{Na_V}\cdot\mathrm{Total}}^{\mathrm{ranvier0}} \times Q_{\bar{g}_{\mathrm{V}}}^{\mathrm{Mainen}}$	8.03×10^{-1}	3.0	9.628	5.13×10^{-1}	$\frac{\mho}{\mathrm{cm}^2}$
	$\bar{g}_{\mathrm{K_V}}^{\mathrm{ranvier0}}$	2.41×10^{-1}	×	×	×	$\frac{\mho}{\mathrm{cm}^2}$
	$\bar{g}_{\mathrm{K_V}}^{\mathrm{ranvier0}} \times Q_{\bar{g}_{\mathrm{V}}}^{\mathrm{Mainen}}$	2.41×10^{-1}	×	×	×	$\frac{\mho}{\mathrm{cm}^2}$
	$R_{\mathrm{Passive}}^{\mathrm{ranvier0}}$	2.24×10^{2}	5.00×10^{1}	5.00×10^{1}	5.00×10^{1}	$\Omega \cdot \mathrm{cm}^2$
	$g_{\mathrm{Passive}}^{\mathrm{ranvier0}}$	4.47×10^{-3}	2.00×10^{-2}	2.00×10^{-2}	2.00×10^{-2}	$\frac{\mho}{\mathrm{cm}^2}$

$g^{\text{ranvier0}}_{\text{Cl}^-,\text{ leak}}$	6.69×10^{-4}	×	×	×	$\frac{\mho}{\mathrm{cm}^2}$
$g^{\text{ranvier0}}_{\text{Na}^+,\text{ leak}}$	7.13×10^{-4}	×	×	×	$\frac{\mho}{\mathrm{cm}^2}$
$g^{\text{ranvier0}}_{\text{K}^+,\text{ leak}}$	3.09×10^{-3}	×	×	×	$\frac{\mho}{\mathrm{cm}^2}$
$I^{\text{ranvier0}}_{\text{MaxPump}}$	4.26×10^{-1}	×	×	×	$\frac{\mathrm{mA}}{\mathrm{cm}^2}$
$V^{\text{ranvier0}}_{\text{m}}$	-69.4	-70.0	-70.0	-70.0	mV
$E^{\text{ranvier0}}_{\text{leak}}$	×	-70.0	-70.0	-70.0	mV
$E^{\text{ranvier0}}_{\text{Cl}}$	-70.0	×	×	×	mV
$E^{\text{ranvier0}}_{\text{Na}}$	60.0	60.0	50.0	60.0	mV
$E^{\text{ranvier0}}_{\text{K}}$	-90.0	-90.0	-90.0	-90.0	mV
$[\text{Cl}^-]^{\text{ranvier0}}_{\text{in}}$	11.0	×	×	×	mM
$[\text{Cl}^-]^{\text{ranvier0}}_{\text{out}}$	151.0	×	×	×	mM
$[\text{Na}^+]^{\text{ranvier0}}_{\text{in}}$	15.0	×	×	×	mM
$[\text{Na}^+]^{\text{ranvier0}}_{\text{out}}$	141.6	×	×	×	mM
$[\text{K}^+]^{\text{ranvier0}}_{\text{in}}$	140.0	×	×	×	mM
$[\text{K}^+]^{\text{ranvier0}}_{\text{out}}$	4.8	×	×	×	mM